Upgrade Report

Jamie Ryan
Mullard Space Science Laboratory
University College London
Surrey, RH13 6NL, UK
jamie.ryan.14@ucl.ac.uk

Contents

1 Sunquakes **2**
1.1 Introduction . . . 2
1.2 Sunquake Observations . . . 3
1.2.1 Sunquake Progenitors . . . 4

2 Eruptive Solar Flares **5**
2.1 An Introduction to the Standard Eruptive Flare Model . . . 5
2.1.1 Solar Atmosphere . . . 6
2.2 Observing Solar Flares . . . 8
2.3 Observable Seismic Signatures . . . 9
2.3.1 Local Helioseismology . . . 9

3 Lower Atmospheric Signatures in a Solar Flare Associated with Seismicity **11**
3.1 Background . . . 11
3.2 Observations . . . 11
3.3 Analysis . . . 13
3.4 Results and Discussion . . . 22
3.5 Future Work . . . 23
3.5.1 In the Last Few Months . . . 23

Appendices **24**

1 Sunquakes

1.1 Introduction

During this age of space-born solar astronomy, understanding the highly dynamic environment of the Sun's atmosphere is a study enriched by a wealth of high detail observations. With each newly launched space instrument the spatial resolution of collected data increases, which coupled with those spacecraft that are tailored to capture light of previously unobserved wavelengths, often leads to new phenomena being observed. Eruptive solar flares fall into this category, in that spacecraft have provided observations that challenge the current theoretical view that the standard eruptive flare model (CSHKP model: (Carmichael, 1964; Sturrock, 1966; Hirayama, 1974; Kopp and Pneuman, 1976) puts forward.

Solar flares are one of the most energetic events to occur in the Sun's atmosphere, where by stored magnetic energy is released in the form of heat, mass motions, and accelerated particles. This highly dynamic process produces many measurable signatures, such as emission from γ-ray to optical wavelengths, a high percentage of which agree with the CSHKP model. However, this is not the full picture. The standard flare model has been modified to include new observations many times over the years (e.g., Shibata and Magara (2011)) and is still unable to describe some observed phenomena. Therefore there is still work to be done before a true account of the complex nature of solar flares can be realised.

Sunquakes are an observable feature during some solar flares that the standard model is unable to explain. It is believed that they are the result of energy and momentum released during the flare impacting the lower solar atmosphere. During a solar flare, energy is released high up in the solar atmosphere and transported down to lower altitudes. If a sufficient amount of momentum impacts the lowest atmospheric layer, then acoustic waves are produced which propagate into sub-surface layers of the Sun and are then observed on the solar surface as a sunquake (see Figure 1a). As acoustic wave-fronts travel into the interior they encounter layers of increasing density causing refraction back toward the solar surface (see Figure 1b). At which point, waves can be observed as circular formations in the surface plasma, expanding outward from a point of origin (see Figure 2).

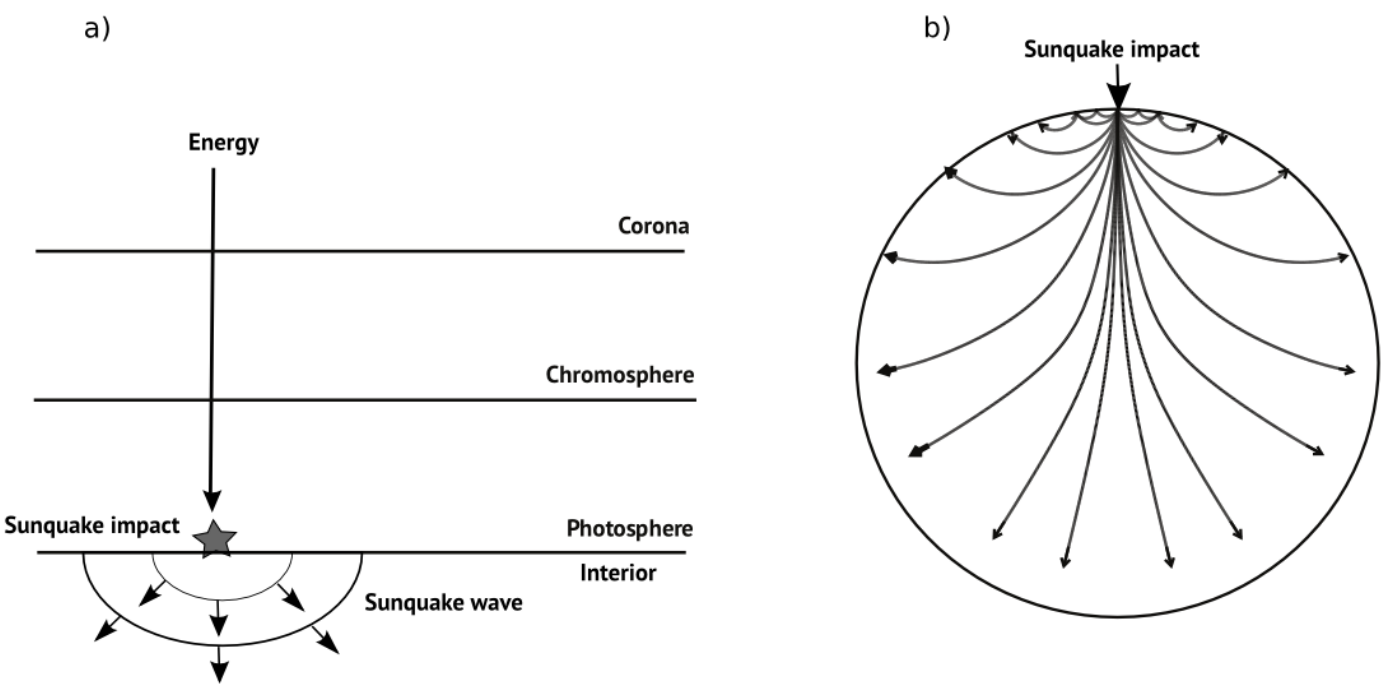

Figure 1: Sunquake cartoon: a) Shows a basic picture of sunquake production. Energy moves down through the solar atmosphere impacting the photosphere and generating a sunquake. b) Shows acoustic wave-fronts propagating into the interior of the Sun. Wave-fronts refract back toward the surface as they encounter increasingly dense sub-surface layers. Waves reaching the surface disturb material in a pattern resembling ripples in a pond. Courtesy of Kosovichev (2014)

1.2 Sunquake Observations

The idea that solar flares can cause acoustic waves inside the Sun was originally put forward by (Wolff, 1972). Wolff made the connection that a large solar flare releasing enough energy to heat the photosphere, would generate expansion of photospheric material, which could lead to an impulsive stimulation of oscillations in the Sun's interior. Wolff also commented that it would be difficult to observe interior oscillations with current (in the 1970s) solar velocity measurement techniques.

A little over twenty years later and Wolff's idea was built upon by Kosovichev and Zharkova (1995), who showed theoretically that acoustic waves in the solar interior could be generated by a large solar flare, and that they may be detectable. A year later and the first detection of a sunquake was made by Kosovichev and Zharkova (1998) during an X class solar flare on July the 9th 1996. Their observational data came from the Solar and Heliospheric Observatory (SOHO) via the Michelson Doppler Imager (MDI) which images the movement of photospheric material by analysing shifts in wavelength of the emitted light. They observed a prominent impulsive downward signature in the Dopplergrams directly over a compact point source which subsequently emanates a set of concentric acoustic waves (see Figure 2). The timing of maximum downward velocity of material derived from the Dopplergrams was out of sync with peak hard x-ray measurements by around a minute. This time delay, coupled with white-light enhancement in the lower atmosphere led to the conclusion that during the flare, accelerated energetic particles heat the cool dense chromosphere causing a shock front which travels downward, depositing energy in lower atmospheric layers, generating a sunquake.

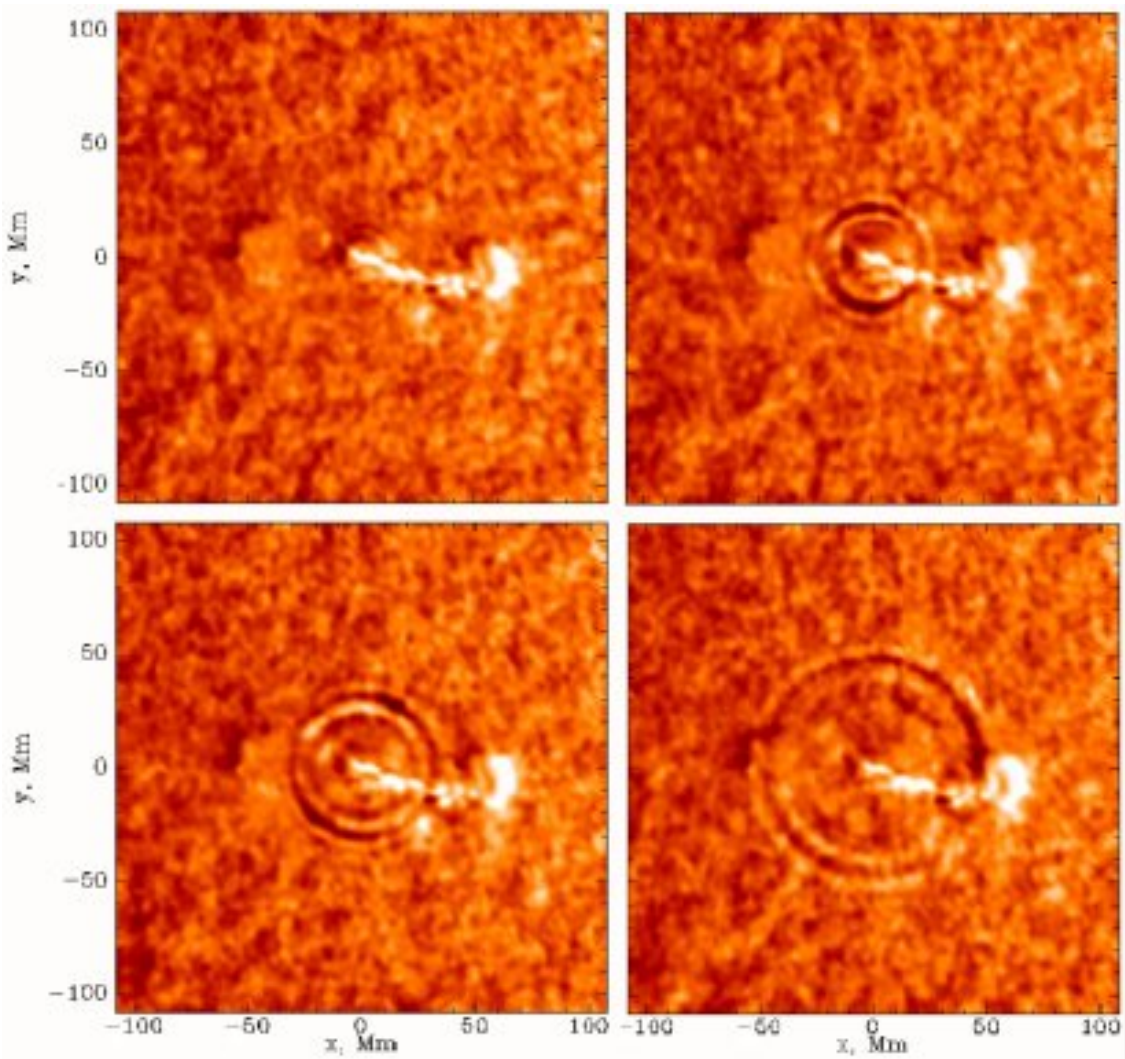

Figure 2: Kosovichev and Zharkova (1998) produced SOHO MDI Dopplergrams from the 1996 July 9th, X class solar flare showing the sunquake expanding outward from it's seismic epicentre to a radial distance of 1.2×10^8 metres. Wave-fronts accelerate from a velocity of 30km/s to 100km/s

The first sunquake observation opened up a whole new area of solar physics, leading to subsequent detections associated other flares. The majority of observations show that sunquakes are often the product of highly

impulsive flares, with the acoustic source aligning spatially with white light enhancement in the lower solar atmosphere and hard x-ray emission in the upper-atmosphere (Donea and Lindsey, 2005; Zharkova and Zharkov, 2007). Donea and Lindsey (2005) went on to calculate the energy needed to stimulate the propagation of an acoustic wave in the sub-photosphere, finding that only $\sim 10^{-3}$ of the energy released by a flare is enough to generate a sunquake. This was an important calculation because it forced the solar community to consider that it might be possible for low energy flares to produce sunquakes, leading to subsequent work by Martínez-Oliveros et al. (2008) looking at seismicity of M-class flares.

A paper by Hudson (2000) put forward for the first time, that sunquake production may depend on the changing configuration of the local magnetic field. This idea was further reinforced by Kosovichev and Zharkova (2001) reporting observations of impulsive changes in magnetic field strength at the photosphere during a solar flare. These magnetic transients were shown to approximately correlate in time and space with hard x-rays, impulsive increases in plasma velocity and increased emission. This line of study was continued (Martínez-Oliveros and Donea, 2009), investigating the magnetic field variation of the photosphere in many flares. The study found that some flares with seismicity do not have a spatial and temporal correlation between sunquakes and magnetic transients. Some flares have magnetic transients and no seismicity, and some flares have a good co-spatial alignment of acoustic activity and magnetic variability. It was noted that the impulsiveness of the magnetic field variation could be important as to whether a sunquake is generated.

Some of the most intriguing of sunquake observations are those that do not abide by the usual set of observable features, in that they are not necessarily associated with hard x-rays and excess white-light emission. For example, a statistical survey carried out by Pedram and Matthews (2012), highlighted a flare containing three footpoints with a seismic source that was co-temporal but not co-spatial with it's closest HXR footpoint; and another source which was co-spatial and co-temporal with its nearest HXR footpoint. This showed that a sunquake does not necessarily correlate with locations of peak emission. Another example by Zharkov et al. (2011) reports an observation of two seismic sources associated with footpoints of an erupting flux rope. During the eruption, the magnetic field above each seismic source undergoes an abrupt permanent reconfiguration. The authors cite the possibility that there exists particle beams low enough in population that HXR emission is undetectable. Further papers investigating the same event (Zharkov et al., 2013) show that there are downward motions of material above the seismic sources and that energy provided by magnetic transients may not be able to account for the acoustic power generated. These observational oddities prove that mechanisms that generate sunquakes are not well understood and there is much research to be done to classify the different progenitors.

1.2.1 Sunquake Progenitors

The progenitors of sunquakes are still unknown and as a result this is an exciting area of research with discoveries still to be made. The general consensus, in terms of valid mechanisms that could cause this phenomenon is an area of contention, however the following progenitors are thought to be at least partly responsible.

- **Radiative backwarming** as a mechanism for producing sunquakes, was first put forward by Donea and Lindsey (2005) to account for a spatial correlation between seismic sources and white light emission from the lower atmosphere. During a solar flare, high energy electrons and impulsively heat the chromosphere and photosphere leading to an enhancement in white light emission (Machado et al., 1989). This WL enhancement can be generated by either; Balmer continuum generated by hydrogen bound-free emission in the upper-chromosphere, which irradiates the photosphere increasing local plasma temperature; H^- emission at deeper altitudes, near the temperature minimum region. In both cases, an impulsive increase in radiation pressure and gas pressure exerted on the photosphere could generate acoustic waves which propagate into the sub-photosphere. Therefore a clear radiative energy contribution from Balmer continuum and general white light emission are considered signatures of radiative backwarming. For backwarming to be responisible for the sunquake, a comparable radiative energy budget in a Balmer or white-light signature would be required.

- **Sudden magnetic field reconfiguration** was first detailed by Hudson et al. (2008). Solar flares are violent physical processes dictated by the interplay between reconnecting magnetic fields and charged solar plasma. If the magnetic field close to the photosphere relaxes to a more horizontal alignment it can impart a Lorentz force on the local plasma environment, resulting in the production of acoustic waves in the sub-photosphere. The key parameter for this mechanism seems to be that the field has to reconfigure

in an sufficiently impulsive manner to generate enough force to induce seismic waves. An observable signature of this progenitor would be impulsive changes in magnetic field strength close to the sunquake.

- **Shocks** are a mechanism originally proposed in initial work by Kosovichev and Zharkova (1995) and Kosovichev and Zharkova (1998), whereby a shock wave propagates from the upper-chromosphere down to lower altitudes. During a solar flare, particles and heat are directed down toward the chromosphere, at which point chromospheric material reacts by increasing in temperature. This increased temperature causes explosive ablation of chromospheric material both upward and downward. The downward component develops into a shock front carrying energy to the lower atmosphere, which can go on to impact the photosphere generating acoustic waves. If the shock is dissipated at higher altitudes such as the lower chromosphere, heat generated during the deposition process can irradiate the photosphere with high energy photons, causing radiative backwarming (Machado et al., 1989). Observational signatures of shocks are red or blue shifted wavelengths which can be captured in Dopplergrams or spectroscopic data.

- **Direct proton collision**, is linked to observations by Zharkova and Zharkov (2007) where the sunquake was spatially aligned with γ-ray emission. γ-rays during a solar flare are an indicator of energetic protons being accelerated along a newly reconfigured magnetic field. Proton beams carry more momentum than electron beams and are able to penetrate through the solar atmosphere to lower altitudes. If an energetic beam of protons makes it down to the photosphere, it can deposit energy in the form of an impact, which due to conservation of momentum could generate acoustic waves in the sub-photosphere. γ-ray data is captured by RHESSI.

2 Eruptive Solar Flares

2.1 An Introduction to the Standard Eruptive Flare Model

Solar flares are the manifestation of magnetic energy release in the form of electromagnetic radiation spanning a wide range of wavelengths. These events are the most energetic phenomena associated with the Sun, with some of the larger flares releasing 10^{37} erg of energy. Flares are classified by the X-ray flux measured by the Geostationary Operational Environmental Satellite (GOES) see Table 1 below.

Classification	Peak Flux Range at 1 to 8 Å ($W.m^{-2}$)
X	10^{-3} - 10^{-4}
M	10^{-4} - 10^{-5}
C	10^{-5} - 10^{-6}
B	10^{-6} - 10^{-7}
A	$< 10^{-7}$

Table 1: shows the GOES flare classification, which is based on powers of ten of hard x-ray flux. X class flares are the most powerful and A class are the weakest.

The exact physical process governing the mechanics of solar flares is not known, however, magnetic reconnection is the currently accepted mechanism. Coronal magnetic loops tethered to sunspots of opposing polarity in the photosphere and sub-photosphere are twisted and stressed by movements of active regions across the solar surface. This shearing of the magnetic field, leads to the build up of magnetic free-energy. This energy can be released when opposing field lines meet and reconnect and the unstable tensioned magnetic field relaxing back to a more stable configuration. As a result stored magnetic energy is converted to radiation, kinetic and thermal energy. The standard 2D flare model is the culmination of research by many authors,(Carmichael, 1964; Sturrock, 1966; Hirayama, 1974; Kopp and Pneuman, 1976), and is still an ongoing area of research that is not entirely understood (Shibata and Magara, 2011). In an active region, a closed magnetic field harbouring a flux rope suddenly opens. As a result, plasma flows along the open field lines from the chromosphere to the corona. This flowing chromospheric material experiences a reduction in plasma pressure which draws together open magnetic field lines of opposing polarity causing reconnection and forming new magnetic loops

at lower altitudes. Reconnection causes excess heating at the peaks of newly connected loops which conducts down toward the chromosphere. Also, particles are accelerated by the new magnetic configuration, flowing to the chromosphere. This injection of thermal energy and accelerated particles heats the chromosphere causing HXR footpoints (Aschwanden et al., 1995) and UV ribbons (Fletcher, 2009). As a result, some chromospheric material evaporates upward into newly created flare loops, whilst some material propagates downward toward the lower chromosphere. The flare loop cools and the process starts again in the next consecutive loop until the unstable magnetic field has relaxed to a state that is closer to it's stable, potential state. In eruptive flares, energy is released every time a new reconnection of a neighbouring loop occurs, this is the reason that flare ribbons appear move away from each other as the flare evolves.

White light flares (WLFs) are associated with the most energetic of solar flares. They occur when flare energy is transported deep into the dense lower atmosphere causing an enhancement in optical wavelengths. It is thought this happens due to an energetic particle beam transporting energy to the lower atmosphere where it's energy dissipates into the dense chromospheric or photospheric material. The collisional thick target model by Brown (1971) says that almost all of the flare energy is carried by the particle beam, therefore, energy dissipated in the lower atmosphere represents a large portion of the flare energy budget. White light enhancement from the lower atmosphere can be explained by either Balmer & Paschen continuum emission from the chromosphere caused by hydrogen recombination, or direct photospheric heating (Ding, 2007) by radiative backwarming (Machado et al., 1989).

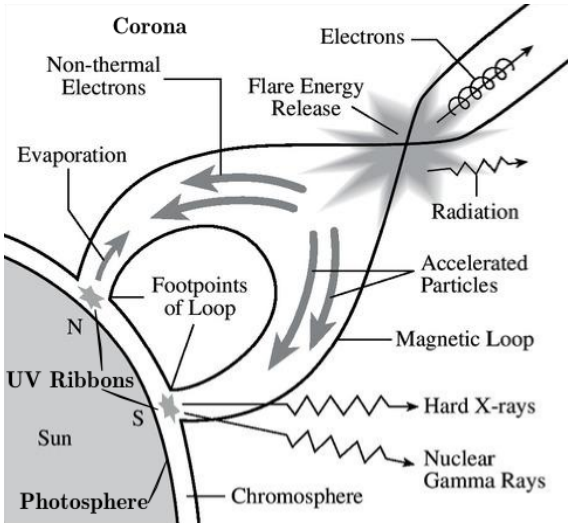

Figure 3: cartoon of the standard 2D solar flare model. Image courtesy of www.tufts.edu

2.1.1 Solar Atmosphere

The solar atmosphere is described as having four main components, the corona, transition region, chromosphere and photosphere, see Figure 4.

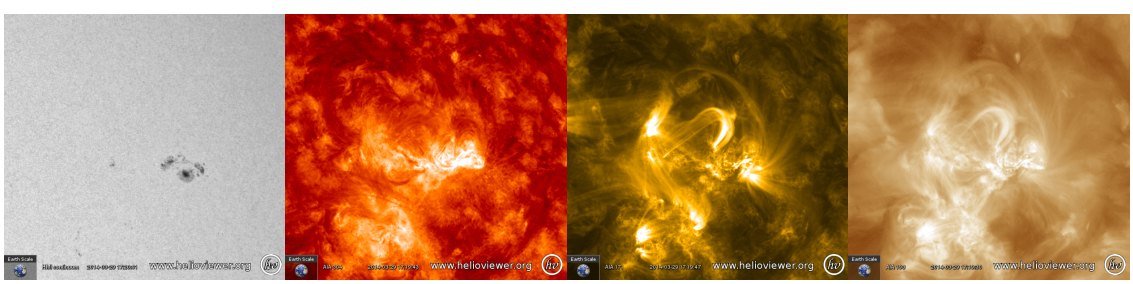

Figure 4: Images taken from the Solar Dynamics Observatory (SDO) instruments, the Helioseismic Magnetic Imager(HMI) and the Atmospheric Imaging Assembly (AIA) displaying the four main components of the solar atmosphere. From left to right layers of the solar atmosphere are increasing in altitude and temperature from the photosphere (SDO/HMI 6173 Å continuum), to the chromosphere (SDO/AIA 304 Å) through the transition region (SDO/AIA 171 Å) then up to the corona (SDO/AIA 193 Å). Images courtesy of www.helioviewer.org

For a sunquake to occur, energy released during a solar flare has to traverse these four layers propagating through nine pressure scale heights as it does so. Pressure scale height is a measure of the distance over which pressure drops off by a factor of e. For example, in the photosphere, $H \sim 150$km, whereas in the corona, $H \sim 100$Mm. The photosphere is where sunquakes form observable wave-fronts and is the lowest in altitude of the four layers. With an effective temperature of $T = 5800$K, the photosphere decreases in temperature with radial distance. If white light enhancement is observed in the photosphere, it is thought to be an indicator of the **Radiative backwarming** progenitor of sunquake generation, which can also be a bi-product caused by chromospheric **Shocks**. The plasma beta (a measure of the ratio between gas and magnetic pressure) in this region is mostly larger than one, $\beta > 1$, meaning plasma pressure is dominant in dictating plasma motions, the exception to this exists in sunspots where $\beta < 1$ and magnetic pressure is dominant.

Found in active regions of the photosphere, sunspots are regions of intense magnetic field playing host to footpoints of loops that can extend out into interplanetary space. They are made up of two main parts, the dark central umbra, surrounded by the slightly less dark penumbra. The umbra hosts magnetic field lines that are tightly packed and pointing radially away from the Sun, whereas the penumbral magnetic field is more horizontal with respect to the solar surface. During a solar flare, coronal loops reconnect causing a reconfiguration of the magnetic field tethered at sunspot locations, at this point, penumbral field lines can collapse toward the photosphere, imparting a Lorentz force on local plasma. This leads to the **Sudden magnetic field reconfiguration** progenitor of sunquake generation. Other features that are found on the photosphere include granules, which are the physical representation of convection currents. Heated plasma rises from below the surface and is seen as the bright central part of the granule, the darker surrounding regions are cooler material sinking back into the interior.

The next region of the atmosphere is the chromosphere which is situated above the photosphere. This layer of plasma is a few thousand kilometres (2000-3000km) thick and is optically thin to visible light so is difficult to see against the brightness of the photosphere. The temperature in this layer increases with height and ranges from 4400K at the temperature minimum region to $\sim 10^5$K at the top, as a result, β drops rapidly crossing unity as it does so. The pressure scale height in this region is changing with altitude. Through the transition region to the corona and the atmosphere starts to heat considerably to $T \sim 10^7$K. This region is visible in white light due to Thompson scattering of photospheric light by free electrons and dust in the coronal magnetic field. The plasma beta is less than one through the entire corona meaning magnetic forces dominate. Figure 5 shows how the solar atmosphere changes with height, temperature and density, giving an indication of the stratification of atmospheric layers. Information in this section is taken from text books: Dwivedi and Parker (2003); Foukal (2004)

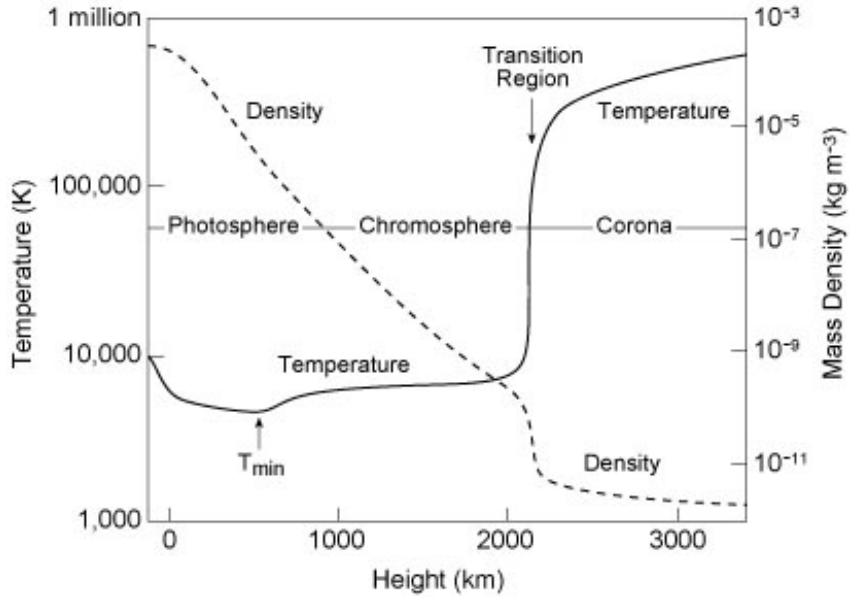

Figure 5: The temperature of the solar atmosphere decreases from values near 6,000 degrees Kelvin at the visible photosphere to a minimum value of roughly 4,400 degrees Kelvin about 500 kilometres higher up. The temperature increases with height, slowly at first, then extremely rapidly in the narrow transition region, less than 100 kilometres thick, between the chromosphere and corona, from about 10^4K to about 10^6K. (Courtesy of Eugene Avrett, Smithsonian Astrophysical Observatory.)

2.2 Observing Solar Flares

Using data collected by spacecraft observing the Sun, energy released during solar flares can be tracked as it is deposited throughout the atmosphere. Energy deposition in the upper chromosphere is marked by HXR footpoints and UV ribbons. The Ramaty High Energy Solar Spectroscopic Imager (RHESSI) observes solar emission ranging from 1 keV X-rays to 20MeV γ-rays produced by energetic particles and nuclear interactions. RHESSI was designed with the aim of understanding impulsive energy release, particle acceleration and transportation in the magnetohydrodynamic environment of the solar atmosphere. Isolating the 10 - 100 keV energy data collected by RHESSI can provide information regarding the intensity and spatial origin of a HXR source. This allows the location of magnetic HXR footpoints to be tracked and the calculation of energy depostion by accelerated electrons.

Observing UV ribbons requires a different spacecraft. The Interface Region Spectroscopic Imager (IRIS) captures near-ultraviolet (NUV) and far-ultraviolet (FUV) emission and is designed to observe the chromosphere at various altitudes. Emission is collected by a slit-jaw imager (SJI) and a spectrometer (SG) simultaneously. The spectrograph is sensitive in both FUV and NUV passbands, which expose 3 CCDs to produce spectra in three UV bands, two FUV and one NUV. Table 2 shows how each passband relates to emission processes occurring from the upper-chromosphere down to the upper-photosphere.

Band	Wavelength Å	Temperature $\log T$	Region of Atmosphere
FUV 1	$1331.7 - 1358.4$	$3.7 - 7.0$	Upper to lower-chromosphere
FUV 2	$1389.0 - 1407.0$	$3.7 - 5.2$	Upper to lower-chromosphere
NUV	$2782.7 - 2851.1$	$3.7 - 4.2$	Chromosphere to upper-photosphere

Table 2: The IRIS/SG is capable of observing three passbands, which relate to different plasma temperatures.

The slit-jaw images, are light collected from a reflective area surrounding the slit. The imager is capable of observing four wavelengths relating to emission at different altitudes as shown by Table 3.

SJI Passband	Wavelength Å	FWHM Å	Temperature $\log T$	Region of Atmosphere
C II	1330	40	$3.7 - 7.0$	Upper-chromosphere
Si IV	1400	40	$3.7 - 5.2$	Upper-chromosphere
Mg II h/k	2796	4	$3.7 - 4.2$	Lower-chromosphere
Mg II wing	2832	4	$3.7 - 3.8$	Upper-photosphere

Table 3: The IRIS/SJ is capable of observing four passbands, which relate to different plasma temperatures.

Signatures from energy deposition in the lowest regions of atmosphere are captured by Solar Dynamics Observatory's (SDO) Helioseismic Imager (HMI), which observes the photosphere. Able to observe optical continuum intensity (6173 Å), helioseismic and magnetic data, SDO/HMI can provide valuable insight into WLFs, sunquakes and magnetic field configuration. Optical continuum data can provide information about WLFs and radiative backwarming of photospheric material, which is a possible sunquake progenitor. Helioseismic data can be used to analyse the movement of material during a solar flare, such as downward flows which could indicate shocks propagating from higher altitudes or particle beams penetrating the atmosphere. The point of origin and wave-fronts of a sunquake can also be detected using helioseismic data, which can be used to calculate acoustic power of the quake. Magnetic data from SDO/HMI shows local magnetic field direction, useful for determining the presence of impulsive changes in magnetic field capable of generating a sunquake.

2.3 Observable Seismic Signatures

Helioseismology is a tool for probing the interior of the Sun. Most techniques in this field of analysis rely on observations of gravity and acoustic waves on the photosphere that are the result of interior excitation. Studying the frequency and modes of these oscillations has revealed much about the internal structure of the Sun. Local helioseismology is a collection of techniques developed for global helioseismology that have been modified for use in studying local regions in higher spatial resolution. The following section provides a very basic introduction to some of these techniques.

2.3.1 Local Helioseismology

Helioseismic Holography Donea et al. (1999) pioneered the use of helioseismic holography to produce seismic images of the solar flare of July 1996 reported to have a sunquake by Kosovichev and Zharkova. Time series egression-power maps at 3.5 and 6 mHz were computed with a 2 mHz bandwidth. It was found that the most powerful acoustic power frequency associated with the flare is centred at 3.5 mHz but has a large amount of noise. However, the 6 mHz range has a much lower ambient noise, therefore producing a better rendering of the seismicity of the flare. It is now standard practice to use the 6 mHz range for helioseismic holographic calculations of egression-power.

Originally the idea of analysing Doppler images of the solar surface in order to observe acoustic sources was put forward by Roddier (1975). Helioseismic holography was developed further in concept by Lindsey and Braun (Lindsey and Braun, 1990; Braun et al., 1992; Lindsey and Braun, 1997) in an effort to to image the solar interior and far-side of the Sun. This technique involves using a Doppler image of a location on the solar surface as a reference wave-field to enable an estimatation of that wave-field at a location in the solar interior at a time preceding or proceeding the image. This is achieved by calculating the ingression or egression of the wave-field by assuming that it's evolution is a, convergence to, or divergence from, the point of origin of that wave-field. The technique uses Green's function (eqn 1, where $\mathbf{r}$ and t are position and time of an observed signal and $\mathbf{r}'$ and t' are the position and time of the signal earlier in time) which assumes that the acoustic wave propagates from a point source, allowing a signal $\psi(\mathbf{r}, t)$ observed on the surface to be devolved backwards in time.

$$G_+(|\mathbf{r} - \mathbf{r}'|, t - t') \tag{1}$$

Where a and b constrain the holographic pupil, equation 2 is then used to devolve the surface signal to calculate the position of subsurface acoustic sources.

$$H_+(\mathbf{r}, z, t) = \int dt' \int_{a<|\mathbf{r}-\mathbf{r}'|<b} d^2\mathbf{r}' G_+(|\mathbf{r} - \mathbf{r}'|, t - t')\psi(\mathbf{r}', t') \tag{2}$$

Equation 3 is then used to calculate the egression power associated with the acoustic sources at a time t.

$$P(z, \mathbf{r}) = \int dt |H_+(\mathbf{r}, z, t)|^2 dt \tag{3}$$

If egression power is required in terms of frequency then equation 3 can be Fourier transformed into frequency space.

Time-Distance The first observation of a sunquake (Kosovichev and Zharkova, 1998) used the time-distance technique to track sunquake wavefronts. The paper by Duvall et al. (1993) explains how to extract time-distance (TD) information from observations of intensity fluctuations on the solar surface. This technique uses travel times of waves between two locations on the solar surface. The method assumes that the travel time of a wave propagating in the interior of the Sun will be modified by any anomalies that it has to travel through, thus the resulting signal will contain the signatures of those irregularities. For instance, if the wave encounters a flow along it's path of travel, it will propagate faster with the flow than against it, affecting travel time. This technique remaps Dopplergrams into polar coordinates, with the point of origin centred on the area of downflowing material during the flare. This remapped image is then Fourier transformed with respect to azimuthal angle, with the resulting image highlighting circular disturbances as a line of positive slope.

3 Lower Atmospheric Signatures in a Solar Flare Associated with Seismicity

3.1 Background

A sunquake is the propagation of acoustic waves in the sub-photosphere, responding to an excitation of the photosphere during the impulsive phase of solar flares. Sunquakes form when energy is deposited in the sub-photosphere, so where does this energy come from? The current view is that the energy required to generate a sunquake is probably delivered by a combination of shocks, radiative backwarming, direct proton collision of the photosphere or sudden magnetic field reconfiguration, see Section 1.2.1. Each of these mechanisms relies on the transport of energy from the corona to the photosphere, and the physical conditions existing in the chromosphere such as magnetic field configuration and plasma density. To understand sunquakes and their relationship to solar flares, we need to understand how energy moves down through the solar atmosphere and the physical conditions that are present.

The majority of the energy released by a flare is deposited in the lower solar atmosphere and manifests itself in the form of enhanced hard X-ray, UV and optical radiation. During the impulsive phase of a solar flare, energy in the form of energetic particles, shocks and MHD waves flow along newly formed coronal magnetic loops, down through the stratified solar atmosphere. As energy is deposited through the differing environments of each atmospheric layer, telltale emission signatures are released. Hard X-ray (HXR) footpoints are observed due to the excitation of the chromosphere by energetic particle beams accelerated by coronal magnetic reconnection during the flare (Aschwanden et al., 1995). According to the standard flare model (Carmichael, 1964; Sturrock, 1966; Hirayama, 1974; Kopp and Pneuman, 1976) magnetic reconnection in the corona leads to energy being directed downward in the form of particles, radiation, MHD waves and conduction of heat, which in turn produces ultra-violet (UV) ribbons in the chromosphere. This means that HXR footpoints and UV ribbons observed in the chromosphere directly map to the reconfiguring magnetic field during the flare. When energy is deposited at lower altitudes such as the photosphere, emission becomes visible in the optical, known as a white light flare (WLF). The processes governing WLF emission in the lower solar atmosphere are detailed by Ding (2007) whereby two main mechanisms are highlighted; Balmer/Paschen continuum emission produced via hydrogen recombination in the lower chromosphere; and enhancement of photospheric continuum emission due to heating of the temperature minimum region. According to Machado et al. (1989), Balmer/Paschen emission upward (i.e., directly detected) also has a downward component which leads to impulsive radiative backwarming of the photosphere which in-turn can generate a sunquake.

3.2 Observations

The X1 flare of the 29th of March 2014 in active region NOAA 12017, was well observed by RHESSI, IRIS and SDO/HMI, collecting HXR, UV and optical emission respectively (see Figure 7). The impulsive phase of the flare occurs at 17:46 UT, at which point all mentioned instruments provide good coverage. RHESSI captured a wide range of high energy emission throughout the flare, see Figure 6. Rhessi flare data from energy bins between 10 and 100 keV are captured from a wide field of view.

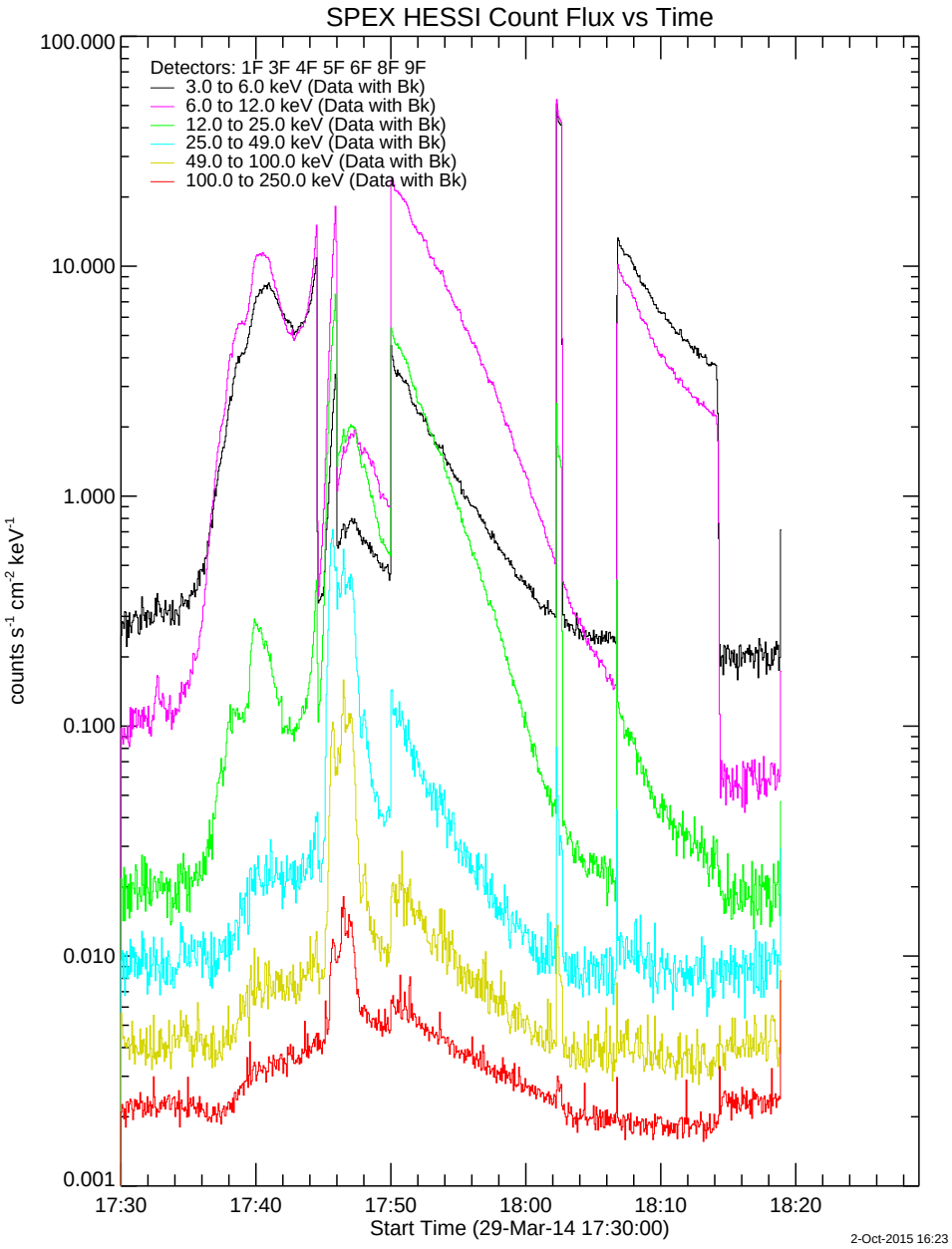

Figure 6: Shows RHESSI counts per area for multiple energy ranges. 3 to 6 keV in black, 6 to 12 keV in pink, 12 to 25 keV in green, 25 to 49 keV in turquoise, 49 to 100 keV in yellow and 100 to 250 keV in red. This range covers both thermal and non-thermal electron processes.

The IRIS spacecraft captured the temporal evolution of the flare between 14:09 and 17:54 UT via it's slit-jaw imager and spectrograph instruments at solar coordinates of 491", 282" with a spatial resolution of 0.1667" per pixel. The slit-jaw imager data provides coverage of a field of view spanning 167" by 174", of passbands that including 1403, 2796 and 2832 Å at 26, 19 and 75 second cadence respectively. The spectrograph slit is aligned directly over chromospheric flare ribbons, and the sunquake point of origin, with a field of view spanning 14" by 174". The spectrograph slit is exposed for ~ 9 seconds at 8 slit locations for a total of 72 seconds cadence. Wavelengths observed over three channels include FUV1: 1331.7 - 1358.4 Å, FUV2: 1389.0 - 1407.0 Å and NUV: 2782.7 - 2851.1 Å, associated with the upper-chromosphere down to the upper-photosphere. Spectral lines include C II, Si IV and Mg II h and k. IRIS data is the standard level 2 data product provided for scientific research, which has been calibrated to negate dark currents, flat-field and spacecraft rotational effects. The HMI instrument onboard SDO observed the entire solar photosphere, collecting 6173 Å continuum intensity data throughout the flare event. HMI has a pixel size of 0.6 " providing reasonable spatial resolution at a cadence of 45 seconds. HMI data is calibrated to negate cosmic-rays, dark currents, flat-field and spacecraft rotational effects. A 6mHZ acoustic egression power map revealing the location of the sunquake is generated via holography techniques (supplied via private communication by Sergei Zharkov). HXR data from RHESSI

and acoustic power data are overlaid on HMI and IRIS slit jaw maps for context, see Figure 7.

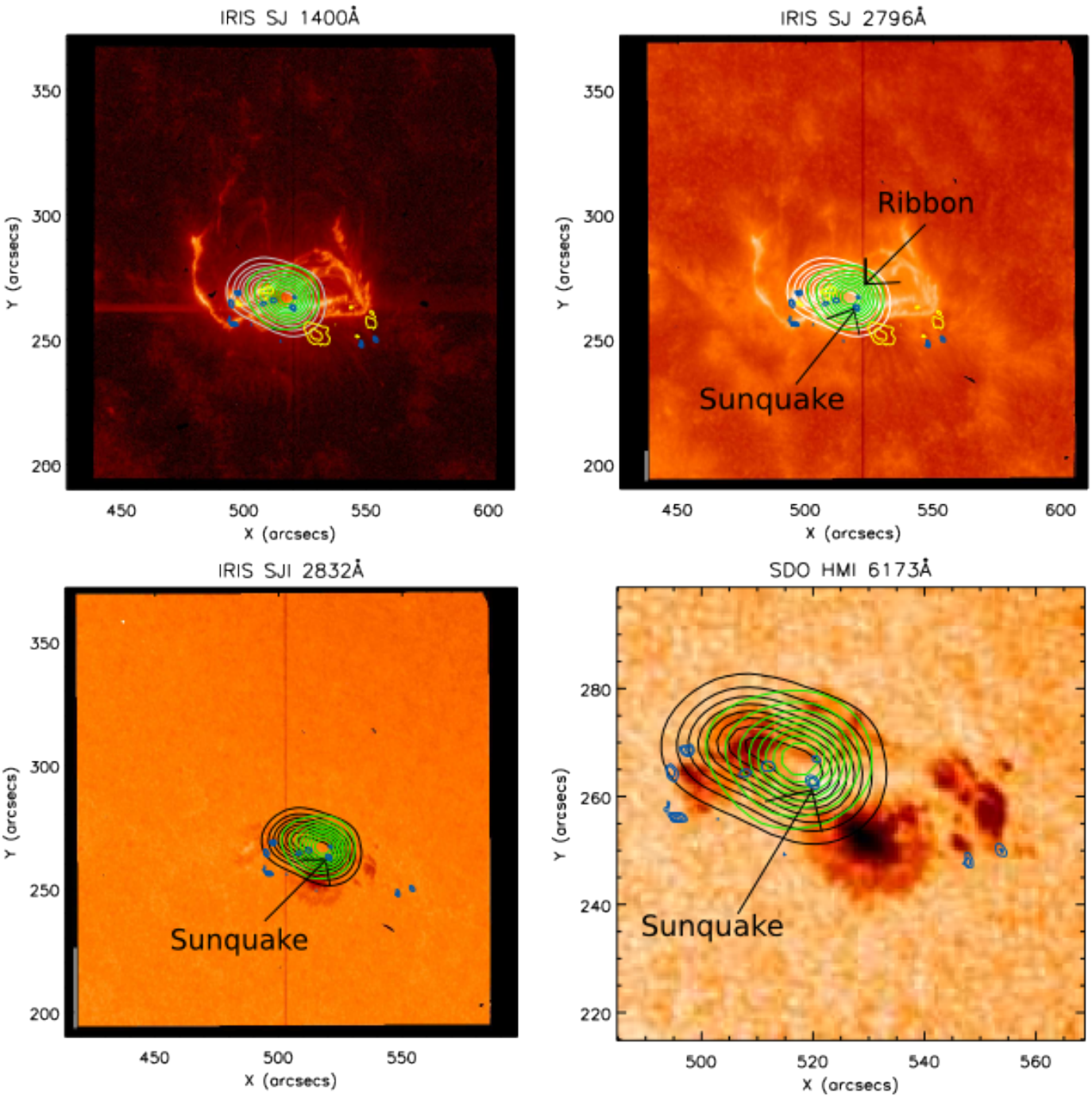

Figure 7: From top left to bottom right, images represent regions of the solar atmosphere at descending altitudes. The top two and bottom left images show IRIS SJ intensity maps of 1403Å (transition Region), 2796Å (chromosphere) and 2832Å (upper-photosphere) data. The bottom right image is SDO HMI 6173Å continuum intensity from the photosphere. Contours show RHESSI HXR with $E = 25 - 50$ keV in white or black and HXR with $E = 50 - 100keV$ in green, sunspot locations in yellow taken from HMI and 6mHz acoustic power in blue.

3.3 Analysis

During the impulsive phase of a flare, high energy emission is an indicator that accelerated particles are present. Assuming that the chromosphere is a thick target (Brown, 1971), then the deposition of energy by accelerated

particles will be by collisions between charged particles and ions producing hard X-ray bremsstrahlung emission.

$$P(E \geq E_c) = \int_{E_C}^{\infty} EF(E)dE \tag{4}$$

The thick target model allows for the integration of the total non-thermal electron power P via equation 4. The electron distribution $F(E)$ is controlled by the power law $AE^{-\delta}$, where E is the electron energy, A is the total injected electron rate normalisation factor, E_C is the low energy cut off and δ is the electron distribution spectral index. Performing the integral gives the total non-thermal electron power in the form of equation 5 .

$$P(E \geq E_c) = \frac{AE_C^{(2-\delta)}}{(\delta - 2)} \tag{5}$$

The value of E_C represents the upper boundary between thermal and non-thermal energy contributions to the x-ray spectrum. This means that the total energy associated with non-thermal electron power calculated by equation 5 is a lower limit.

Using the `ospex` software within SolarSoft (SSWIDL) RHESSI data are fit using the thick target non-thermal electron model. The entire data set has to be split into short intervals to improve the accuracy of fitting and the detail of resulting plots. Also the attenuator state of the instrument has to be taken into account due to differences in sensitivity to incoming photons. Therefore it is important to define intervals for fitting first by the attenuator state as `ospex` will mitigate for the differences in count sensitivity. Shown in Figure 8 is the resulting fit over the majority of the impulsive phase of the flare. At the peak of the impulsive phase between 17:46 and 17:47 the RHESSI fit shows an energy ranging from 1.0×10^{28} to 2.5×10^{29} erg. Assuming the fitting model is correct then the release of this energy is due to non-thermal electrons being accelerated and depositing energy into the chromosphere.

RHESSI 10 - 100 keV Hard Xray Energy Over Time

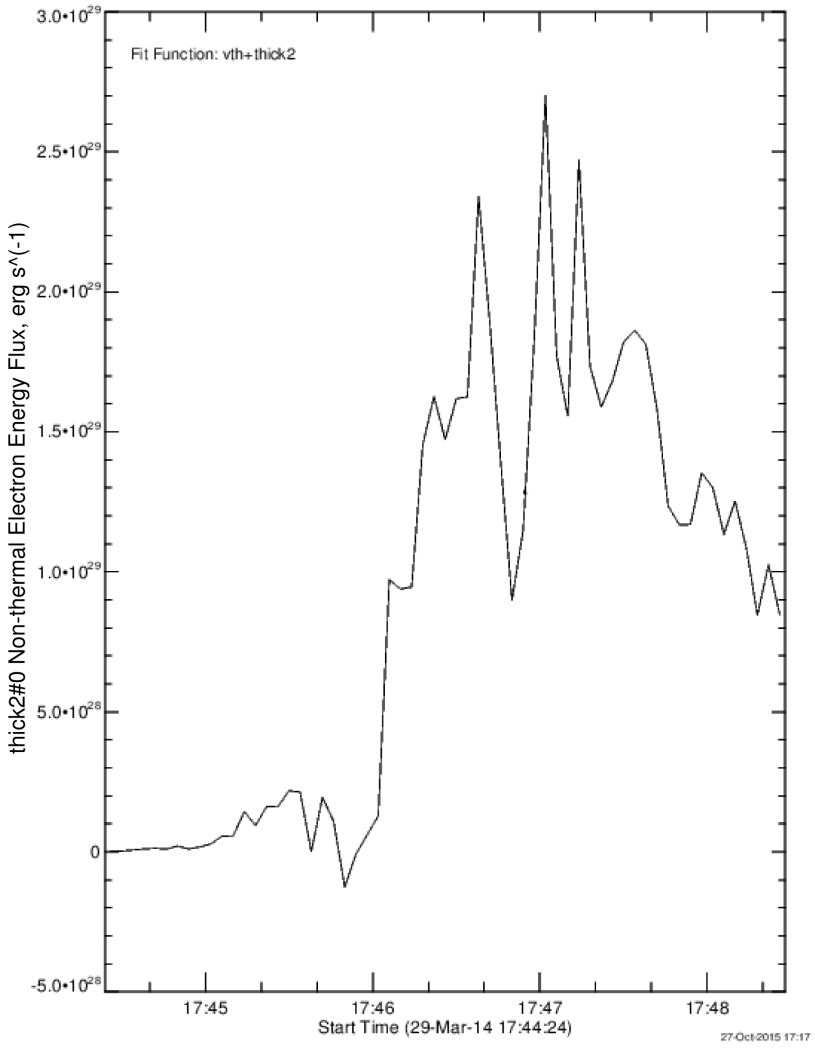

Figure 8: Shows the energy evolution of hard x-ray emission collected by RHESSI 10 to 100 keV bins. Energy units are calculated by fitting a non-thermal electron model to the data.

White light flares are difficult to see against the bright photospheric background therefore to maximise the insight gained from observations of the flaring photosphere, data must be filtered. Silimarly to Kerr and Fletcher (2014), photospheric data captured by IRIS MG II wing slit-jaw and SDO HMI continuum observations are subjected to a running difference filter to isolate locations that are white-light enhanced. The running difference filter effectively removes static features leaving behind those pixels that are changing over short time-scales. However, for removing signatures of those processes occurring over shorter time periods such as granulation and p-mode oscillations, this filtering technique is ineffective. This is not a problem, as for the purpose of white light flare analysis, the data yield a strong contrast between flare-enhanced and background pixels after being filtered by a $i - 2$ running difference. The next stage is to determine which pixels in the difference image are those that are enhanced during the flare. For the best result, white-light enhanced pixels are identified using a combination of visual inspection and thresholding. Attempts at automating the identification process tend to lead to false positives being triggered by noise or granulation features. IRIS SJIs and SG data have no need for filtering.

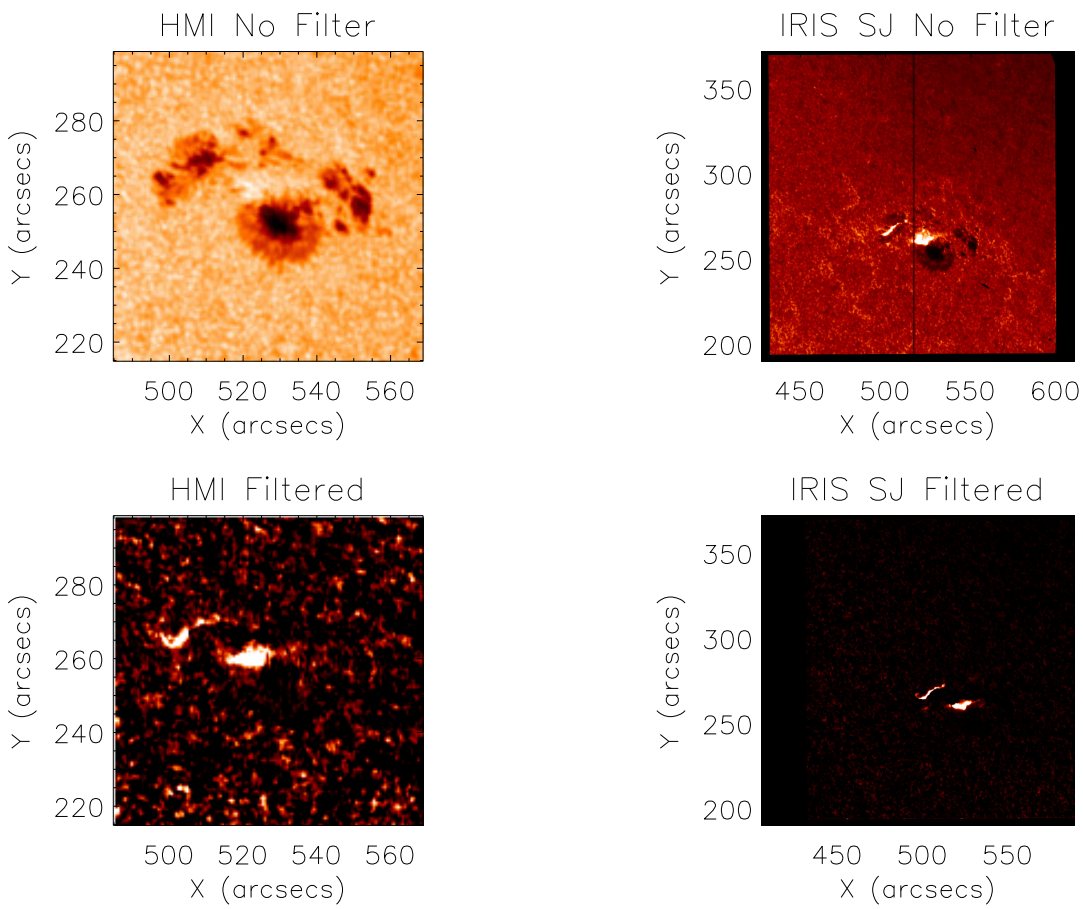

Figure 9: White light flares are difficult to observe against the bright photosphere requiring processing with a running difference filter to enhance ribbon features. The figure shows IRIS SJ 2832 Å and SDO HMI continuum data before (top) and after (bottom) filtering.

IRIS SJ and SG data are converted from relative intensity (DN per pixel) to energy (erg) units using conversion factors. Provided in the instrument documentation (De Pontieu et al., 2014) is a method for acquiring the conversion factors in SSWIDL. It is then a case of inserting IRIS DN per pixel intensity values into the equation 6. F_{DN} is flux in units of DN per pixel, C_{d2p} is the DN to photon conversion factor, E_λ is the photon energy and E_{erg} is to put the result into erg units.

$$E = \frac{F_{DN} C_{d2p} E_\lambda}{E_{erg}} \tag{6}$$

To perform the same conversion for SDO HMI data required a slightly different approach due to the non-existent DN to photon conversion factor. Using a combination of sources (Boerner et al., 2012; Couvidat et al., 2012) the instrument's properties are used to fulfil a conversion factor in the form of equation 7. Where g is the instrument gain, QE is the quantum efficiency of the charged couple device and A_{ap} is the instrument aperture area, all other terms hold the same meaning as in equation 6.

$$E = \frac{F_{DN} E_\lambda}{g Q E A_{ap} E_{erg}} \tag{7}$$

For the IRIS and SDO HMI data sets, multiple sample points have been chosen based on locations specific to the sunquake and ribbon activity. Figures 10, 11, 12 and 13 show the ribbon coordinates sampled from each data set. Studying the flare in this way allows the energy distribution along the ribbon to be analysed and provides a point of comparison for the sunquake location. Each data set has five sample points per ribbon, a procedure which is repeated at two time frames, 17:45 and 17:46, providing twenty individual energy measurements per data set. The number of sample points will likely be increased in the future to provide better spatial resolution for ribbon energy distribution analysis. The problem with defining multiple ribbon samples over five different data sets comes when one considers the morphology of the local magnetic field. Accelerated charged material

can only travel along the magnetic field, so the shape of those field lines will dictate the location of emission therefore the morphology of the ribbon. With this in mind the sample of coordinates chosen is based on matching common morphological features seen in each data set.

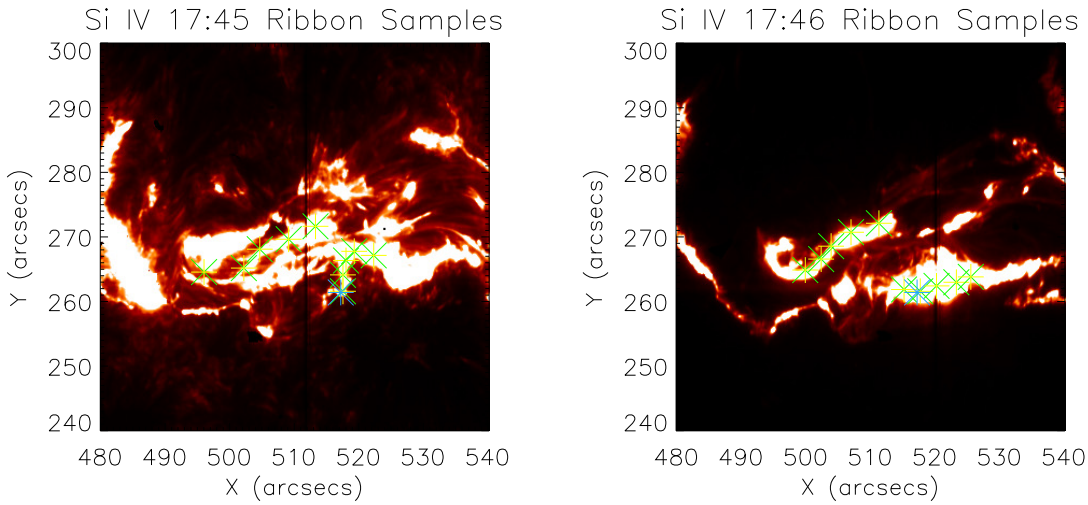

Figure 10: Shows IRIS Si IV slit-jaw data with sampled ribbon and sunquake pixel coordinates marked in green and blue respectively. Twenty ribbon sample points are taken from two instances in time.

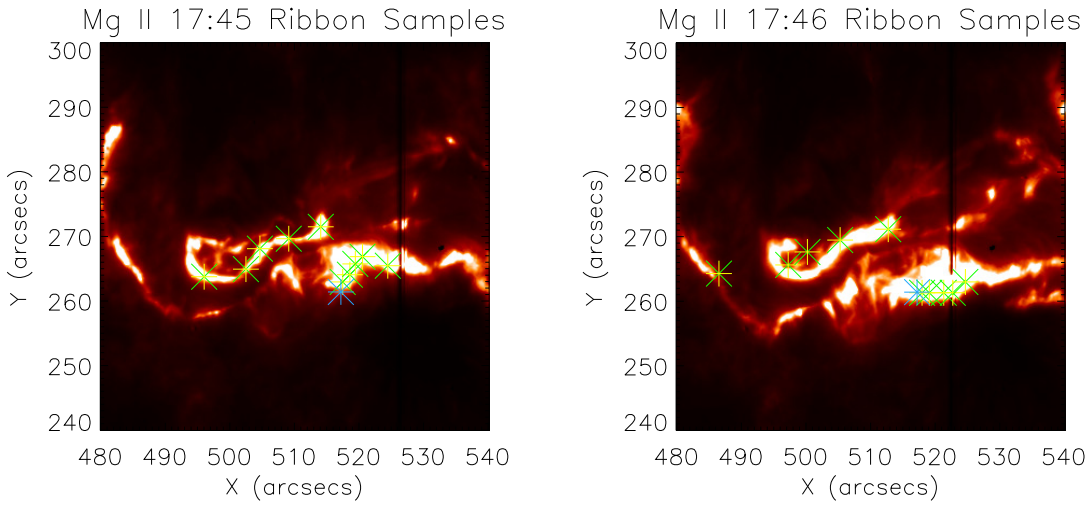

Figure 11: Shows IRIS Mg II slit-jaw data with sampled ribbon and sunquake pixel coordinates marked in green and blue respectively. Twenty ribbon sample points are taken from two instances in time.

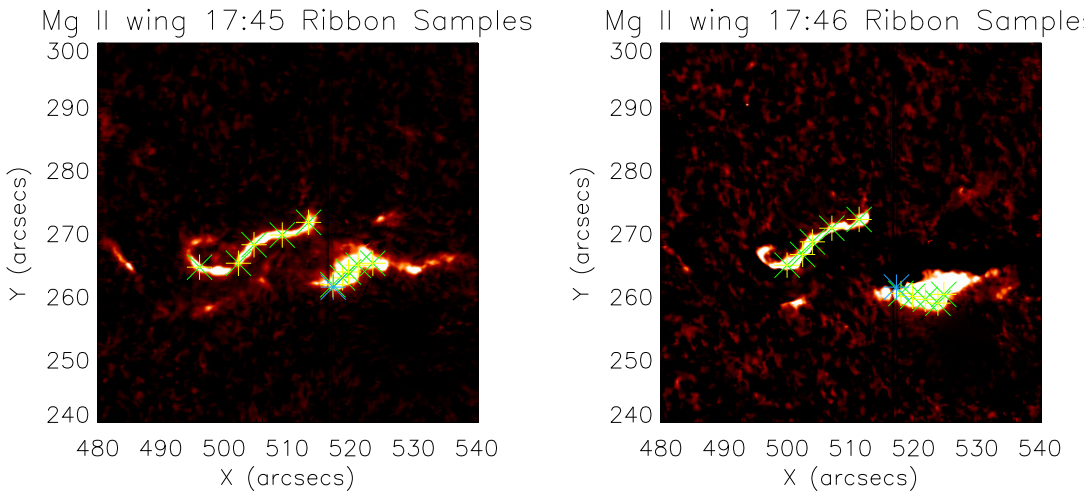

Figure 12: Shows IRIS Mg II wing slit-jaw data with sampled ribbon and sunquake pixel coordinates marked in green and blue respectively. Twenty ribbon sample points are taken from two instances in time.

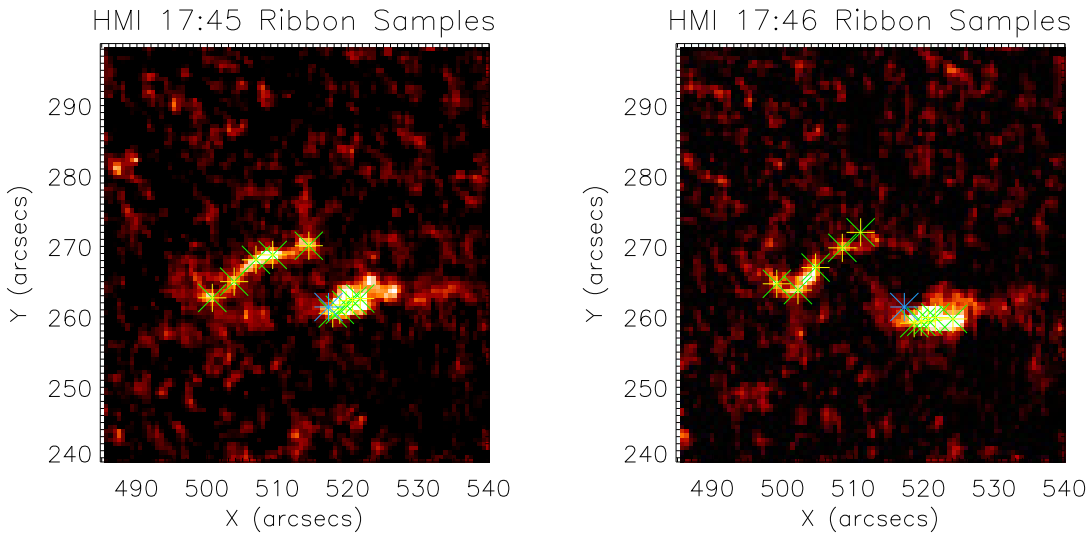

Figure 13: Shows SDO HMI continuum with sampled ribbon and sunquake pixel coordinates marked in green and blue respectively. Twenty ribbon sample points are taken from two instances in time. This procedure is also applied to IRIS SJ and SG data, see the Appendix for more figures.

IRIS spectroscopic data is sampled over a wavelength range of 2825.7 and 2825.8Å (see 14) which is within the Balmer continuum. Balmer Data is sampled at slit positions and pixels that relate to one quake position and twenty ribbon samples, as with the other data sets.

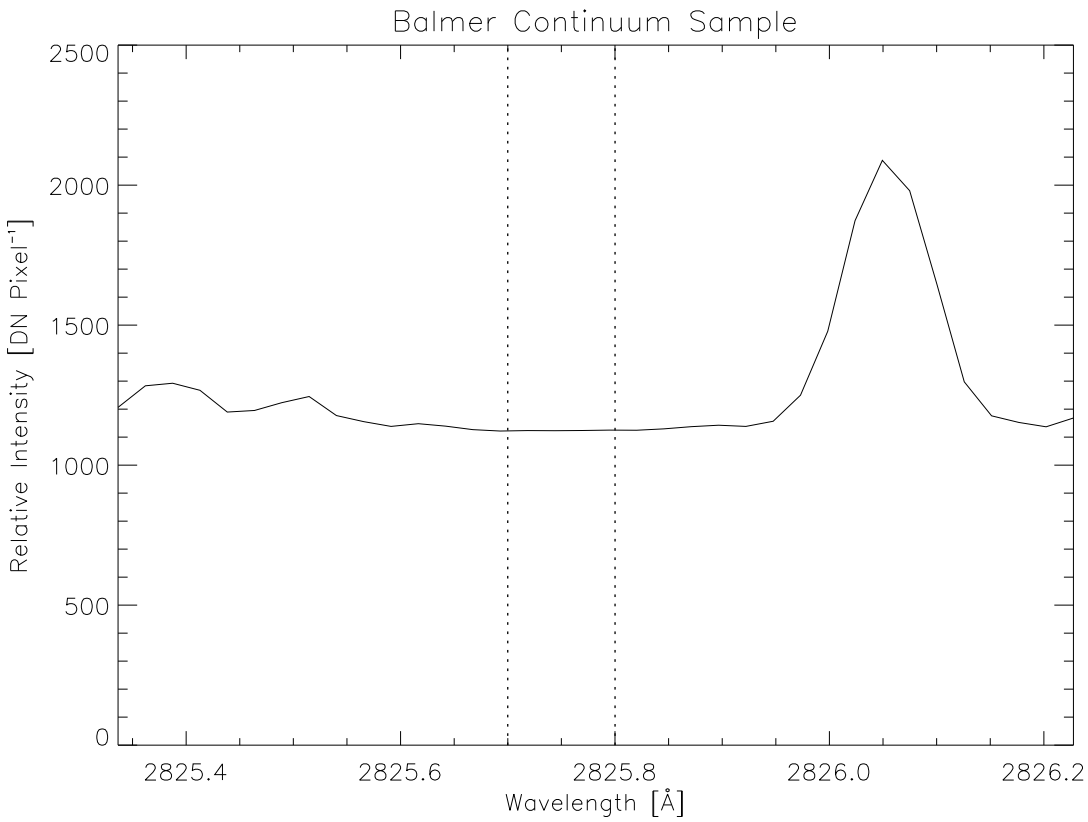

Figure 14: Shows the Balmer continuum component sampled from the IRIS SG data. Balmer emission is an indicator of radiative backwarming of the photosphere.

Once all energies are calculated for each location and data set, time series energy-curves are created, see Figures 8 and 16 (the Appendix contains the energy curves taken from ribbon locations). Each energy-time ladder plot contains energy curves from IRIS SJ 1400 Å 2796 Å SG Balmer, SJ 2832 Å and SDO HMI continuum aligned in time. From top to bottom, the order of the plots in the ladder represents descending plasma temperature in the solar atmosphere see Tables 2 and 3. Tables 4 and 5 display energy values taken from each pixel location and data set, except RHESSI, at two times corresponding to maximum WLF ribbon intensity at 17:45 and 17:46. Figure 16 contains plots for the sunquake epicentre pixel, peak energies from each data set range from 9.63×10^{14} erg from IRIS 1400 Å 4.36×10^{16} erg from IRIS 2796 Å which is a lower limit due to over saturation of the instrument CCD, 2.68×10^{16} erg from IRIS Balmer, 8.21×10^{15} erg from IRIS 2832 Å and 3.29×10^{13} erg from SDO HMI continuum.

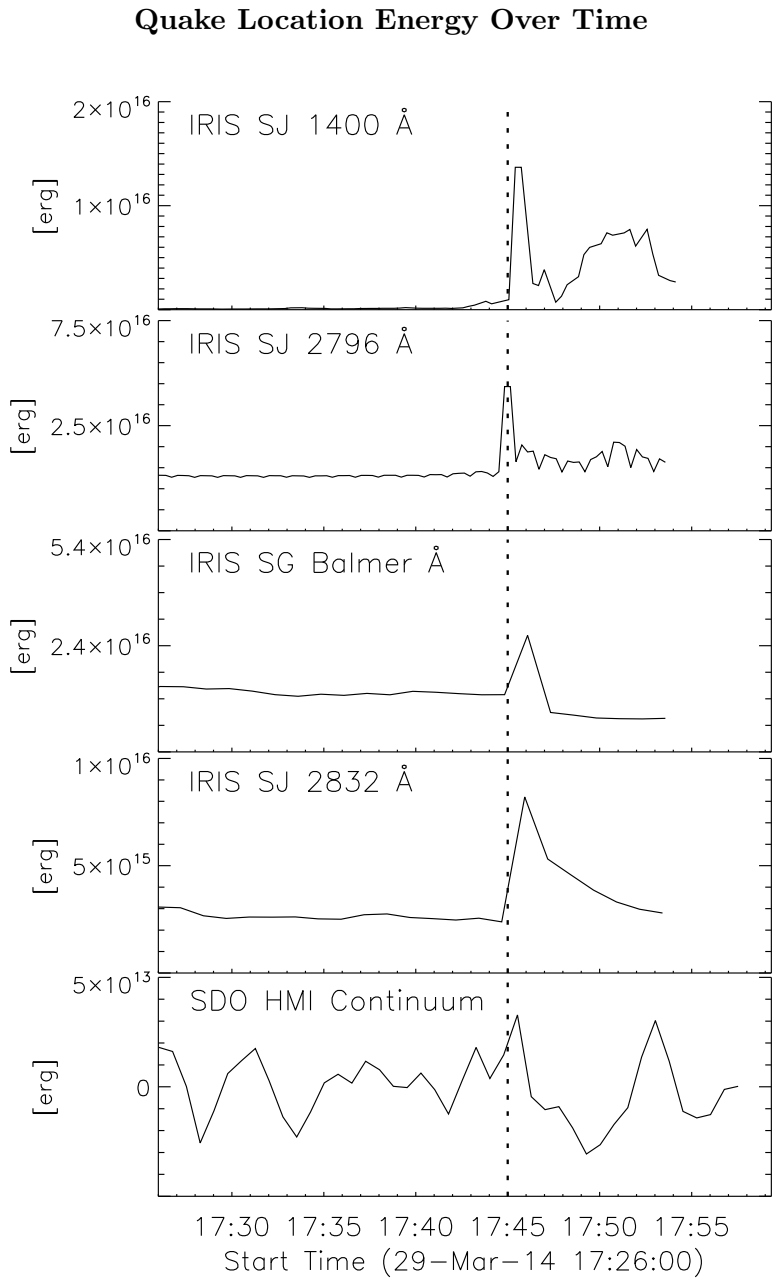

Figure 15: Shows calculated energy values over time of the region thought to be the sunquake epicentre (518.5", 264.0"). Each plot represents an independent data set, in order from top to bottom the sets are; IRIS SJ 1400 Å (Si IV); IRIS SJ 2796 Å (Mg II); IRIS SG 2825.7 to 2825.8 Å (Balmer Continuum);IRIS SJ 2832 Å (Mg II wing); SDO HMI continuum (HMI). The dotted line running vertically through each plot signifies a the onset time of the eruptive phase of the flare

Ribbon plots show a wide range of properties. In an order dictated by Table 5. The following is a bulletized summary of each ribbon position ladder-plot. The ribbon location is based on the HMI coordinates.

- Figure 17 shows ribbon location 517.800, 260.500. Comparing peak energies from each data set to the sunquake pixel, this location shows; Si IV has 1.9 times more energy ; Mg II has 2 times more energy; Balmer has 0.47 of the energy; Mg II wing has 1.1 times more energy; HMI continuum has 2 times more energy.

- Figure 18 shows ribbon location 518.800, 261.000. Comparing peak energies from each data set to the sunquake pixel, this location shows; Si IV has 0.4 of the energy; Mg II has 0.65 of the energy; Balmer has 0.74 of the energy; Mg II wing has 1.03 times more energy; HMI continuum has 3.5 times more energy.

- Figure 19 shows ribbon location 519.700, 261.700. Comparing peak energies from each data set to the

sunquake pixel, this location shows; Si IV is saturated; Mg II is saturated; Balmer has 0.33 of the energy; Mg II wing has 2.8 times more energy; HMI continuum has 4.98 times more energy.

- Figure 20 shows ribbon location 520.600, 262.300. Comparing peak energies from each data set to the sunquake pixel, this location shows; Si IV is saturated; Mg II has 0.36 of the energy; Balmer has 0.26 of the energy; Mg II wing has 0.94 of the energy; HMI continuum has 4.50 times more energy.
- Figure 21 shows ribbon location 521.700, 262.600. Comparing peak energies from each data set to the sunquake pixel, this location shows; Si IV is saturated but shows at least 14.2 times more energy; Mg II is saturated; Balmer has 0.21 of the energy; Mg II wing has 1.08 times more energy; HMI continuum has 3.56 times more energy.
- Figure 22 shows ribbon location 500.700, 262.700. Comparing peak energies from each data set to the sunquake pixel, this location shows; Si IV is saturated; Mg II is saturated; Balmer has 0.42 of the energy; Mg II wing has 0.72 of the energy; HMI continuum has 2.02 times more energy.
- Figure 23 shows ribbon location 503.800, 265.000. Comparing peak energies from each data set to the sunquake pixel, this location shows; Si IV has 2.79; Mg II is saturated; Balmer has 0.21 of the energy; Mg II wing has 1.08 times more energy; HMI continuum has 3.56 times more energy.
- Figure 24 shows ribbon location 506.900, 268.100. Comparing peak energies from each data set to the sunquake pixel, this location shows; Si IV is saturated; Mg II is saturated; Balmer has 0.13 of the energy; Mg II wing has 0.54 of the energy; HMI continuum has 2.40 times more energy.
- Figure 25 shows ribbon location 509.277, 268.792. Comparing peak energies from each data set to the sunquake pixel, this location shows; Si IV is saturated; Mg II is saturated; Balmer has 0.07 of the energy; Mg II wing has 0.48 of the energy; HMI continuum has 3.04 times more energy.
- Figure 26 shows ribbon location 514.400, 270.100. Comparing peak energies from each data set to the sunquake pixel, this location shows; Si IV is saturated; Mg II is saturated; Balmer has 0.12 of the energy; Mg II wing has 0.85 of the energy; HMI continuum has 1.5 times more energy.
- Figure 27 shows ribbon location 518.600, 259.100. Comparing peak energies from each data set to the sunquake pixel, this location shows; Si IV has 2.50 times more energy; Mg II is saturated; Balmer has 0.82 of the energy; Mg II wing has 2.02 times more energy; HMI continuum has 1.68 times more energy.
- Figure 28 shows ribbon location 519.600, 259.300. Comparing peak energies from each data set to the sunquake pixel, this location shows; Si IV has 0.5 of the energy; Mg II has 0.3 of the energy; Balmer has 1.01 times more energy; Mg II wing has 3.01 times more energy; HMI continuum has 2.51 times more energy.
- Figure 29 shows ribbon location 520.600, 259.500. Comparing peak energies from each data set to the sunquake pixel, this location shows; Si IV has 2.3 times more energy; Mg II has 0.4 of the energy; Balmer has 1.80 times more energy; Mg II wing has 2.15 times more energy; HMI continuum has 3.77 times more energy.
- Figure 30 shows ribbon location 521.600, 259.900. Comparing peak energies from each data set to the sunquake pixel, this location shows; Si IV has 0.63 of the energy; Mg II has 0.28 of the energy; Balmer has 0.60 of the energy; Mg II wing has 2.37 times more energy; HMI continuum has 5.25 times more energy.
- Figure 31 shows ribbon location 524.100, 259.700. Comparing peak energies from each data set to the sunquake pixel, this location shows; Si IV is saturated; Mg II has 0.55 of the energy; Balmer has 1.26 times more energy; Mg II wing has 1.74 times more energy; HMI continuum has 3.27 times more energy.
- Figure 32 shows ribbon location 499.100, 264.700. Comparing peak energies from each data set to the sunquake pixel, this location shows; Si IV is saturated; Mg II has 0.15 of the energy; Balmer has 0.9 of the energy; Mg II wing has 2.84 times more energy; HMI continuum has 1.90 times more energy.
- Figure 33 shows ribbon location 502.100, 263.800. Comparing peak energies from each data set to the sunquake pixel, this location shows; Si IV is saturated; Mg II is saturated; Balmer has 0.72 of the energy; Mg II wing has 1.65 times more energy; HMI continuum has 2.32 times more energy.

- Figure 34 shows ribbon location 504.600, 267.000. Comparing peak energies from each data set to the sunquake pixel, this location shows; Si IV is saturated; Mg II is saturated; Balmer has 0.79 of the energy; Mg II wing has 2.11 times more energy; HMI continuum has 2.48 times more energy.

- Figure 35 shows ribbon location 508.400, 269.800. Comparing peak energies from each data set to the sunquake pixel, this location shows; Si IV is saturated; Mg II is saturated; Balmer has 0.41 of the energy; Mg II wing has 0.98 times more energy; HMI continuum has 1.71 times more energy.

- Figure 36 shows ribbon location 511.000, 272.000. Comparing peak energies from each data set to the sunquake pixel, this location shows; Si IV is saturated; Mg II is saturated; Balmer has 0.39 of the energy; Mg II wing has 0.67 of the energy; HMI continuum has 0.67 times more energy.

Another consideration is that Figure 16 only relates to one pixel, therefore to analyse the energy emitted from an area comparable to the sunquake origin area would provide a better estimate of the radiative energy available. This has been calculated for HMI continuum data only, based on the sunquake area 2.6×10^{16} cm^2 as stated in Judge et al. (2014). Based on this area value 13 HMI pixels are sampled, summed and converted to energy, producing an upper limit of 2.54×10^{17} erg. Comparing this to the sunquake energy, $1.3 \pm 0.05\times10^{26}$ $erg.s^{-1}$, also stated in Judge et al. (2014) to the hmi area estimate shows that the sunquake contains 10^9 times more energy.

3.4 Results and Discussion

This project presents a first look at a multi-wavelength energy analysis of the lower solar atmosphere during the 29th of March 2014 X class solar flare. The main focus up to this point has been to acquire energy estimates from the various atmospheric regions in an attempt to assess the likelihood of radiative backwarming as a generation method for the sunquake. The location of maximum acoustic power, RHESSI HXR, IRIS and SDO intensity correlate both spatially and temporally (see Figure 7), showing that energy input into the upper chromosphere via accelerated non-thermal electrons propagates down to the photosphere. The sunquake is located directly underneath both maximum HXR and an area of white-light emission.

Energy estimates from RHESSI data show there to be between 1.0×10^{28} to 2.5×10^{29} erg during the impulsive phase of the flare. Comparing this to the sunquake energy of $1.3 \pm 0.05\times10^{26}$ $erg.s^{-1}$ means that the acoustic energy is well within the energy budget provided by accelerated non-thermal electrons, so how is the energy getting to the photosphere to cause seismic event?

Energy estimates from IRIS are not always useful due to over saturation of the instrument CCD, however, when comparing the ribbon locations to that of the sunquake some clear behaviours reveal themselves. The 1400 Å channel is almost always showing greater radiative energy in all ribbon locations compared to the sunquake. This could be because transition region ribbons are rarely directly above the sunquake epicentre due to magnetic field configuration. The 2796 Å channel becomes saturated slightly less often than the 1400 Å providing more insight. The IRIS 2796 Å channel is less in energy than the sunquake location around 30% of the time. However, no real comparison can be attained due to the saturation of the CCD at the majority of ribbon pixels and the sunquake pixel. The only information that can be deduced, is that the sunquake pixel has an extraordinary 2796 Å enhancement but then so do the majority of the ribbon locations. Balmer emission calculated from IRIS SG data is consistently of less energy than at the sunquake location, this is an interesting result as it means that there is more radiative backwarming above the sunquake pixel than in any other location sampled. However, the energy required to generate the sunquake is in the order of 10^25 ergs, which when compared to the 2.68×10^{16} erg of energy available in the Balmer pixel is 10^9 times greater! Perhaps radiative backwarming only plays a bit-part in the generation of the sunquake? The 2832 Å IRIS channel is harder to summarise due to the fact that comparing ribbon locations to that of the sunquake show that there is a 50:50 chance that the ribbon could have greater or lower energy output. SDO HMI continuum data is probably the most revealing, in that almost all of the ribbon locations have far greater energy output than the sunquake location. This could be explained by the sunquake being only partially under a white light ribbon.

In conclusion, this analysis has barely scratched the surface of the information available in the data. Some immediate trends have been noticed such as the lower levels of Balmer and higher levels of photospheric continuum energy in the flare ribbons compared to the sunquake. Is there a connection between these two emission regions, and do these signatures have anything to do with the generation of the sunquake? In general the data sets available are tending to show that there is not enough energy in atmospheric emission to generate the sunquake via radiative backwarming.

3.5 Future Work

Obviously there is a need for a much more detailed analysis, which will be the main task for the immediate future. Plotting energy behaviours of each ribbon location and data set would help to visualise the trends discussed. There is plans to analyse γ-ray and magnetogram data to look for signatures associated with direct particle collision and impulsive magnetic field reconfiguration respectively. IRIS SG data will be used to analyse Doppler-shift to look for shock waves.

3.5.1 In the Last Few Months

The majority of the work carried out since the last panel meeting has been:

- Calculate energy associated with emission captured by HMI to compare with the acoustic power of the sunquake.
- Calculate energy associated with emission captured by IRIS slit jaw and spectrometer in order to estimate energy deposition in the atmosphere.
- Calculate energy associated with Balmer emission to assess likely energy contribution of radiative back-warming.
- Calculate non-thermal electron power via HXR spectra to estimate the initial energy of the electron beam accelerated by the corona.

Appendices

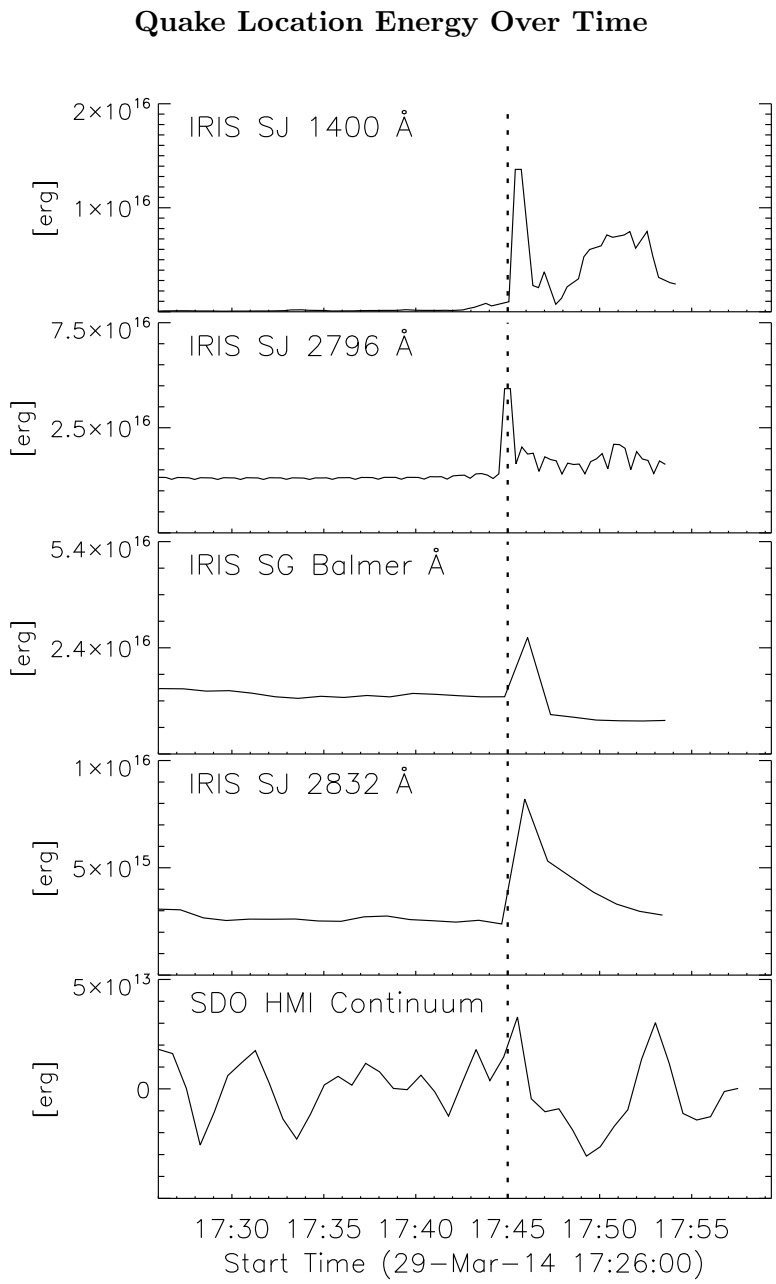

Figure 16: Shows calculated energy values over time of the region thought to be the sunquake epicenter (518.5", 264.0"). Each plot represents an independant data set, in order from top to bottom the sets are; IRIS SJ 1400 Å (Si IV); IRIS SJ 2796 Å (Mg II); IRIS SG 2825.7 to 2825.8 Å (Balmer Continuum);IRIS SJ 2832 Å (Mg II wing); SDO HMI continuum (HMI).

Energy Over Time, Ribbon Location: x = 517, y = 260

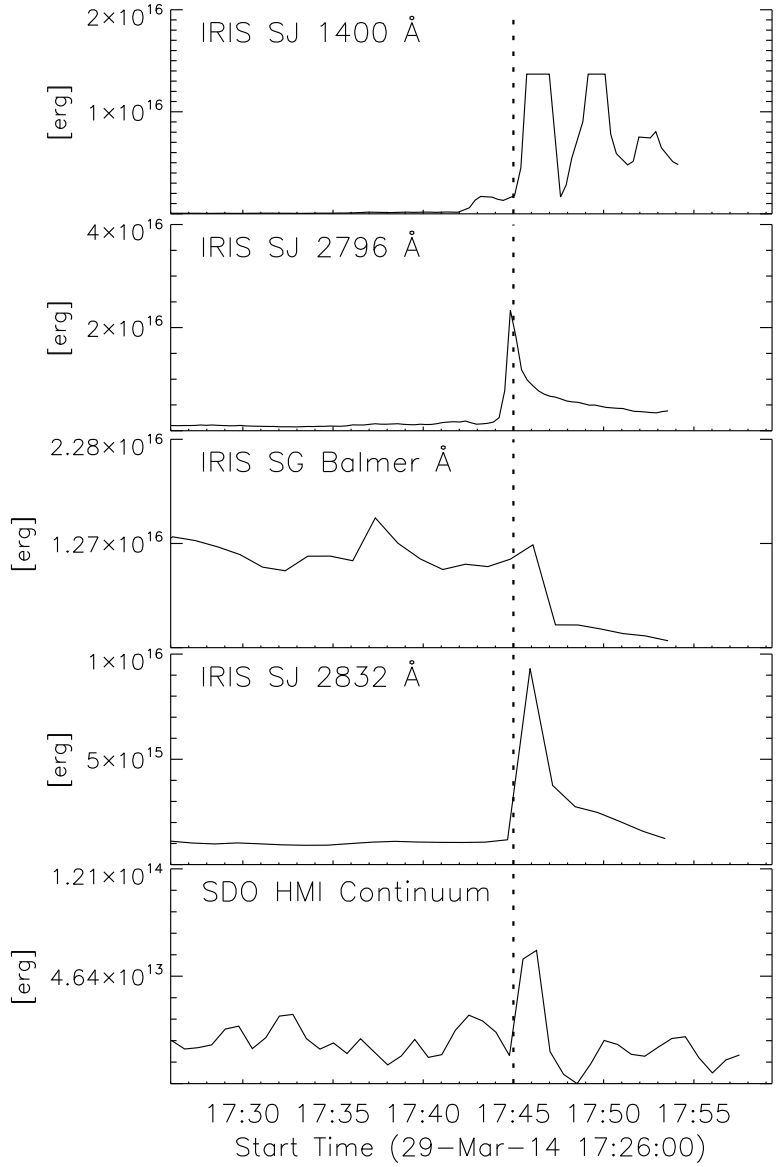

Figure 17: Shows calculated energy (erg) values over time (UT) for the heliocentric coordinates (arcsec) contained in the plot title. Each plot represents an independant data set, in order from top to bottom the sets are; IRIS SJ 1400 Å (Si IV); IRIS SJ 2796 Å (Mg II); IRIS SG 2825.7 to 2825.8 Å (Balmer Continuum);IRIS SJ 2832 Å (Mg II wing); SDO HMI continuum (HMI).

Energy Over Time, Ribbon Location: x = 518, y = 261

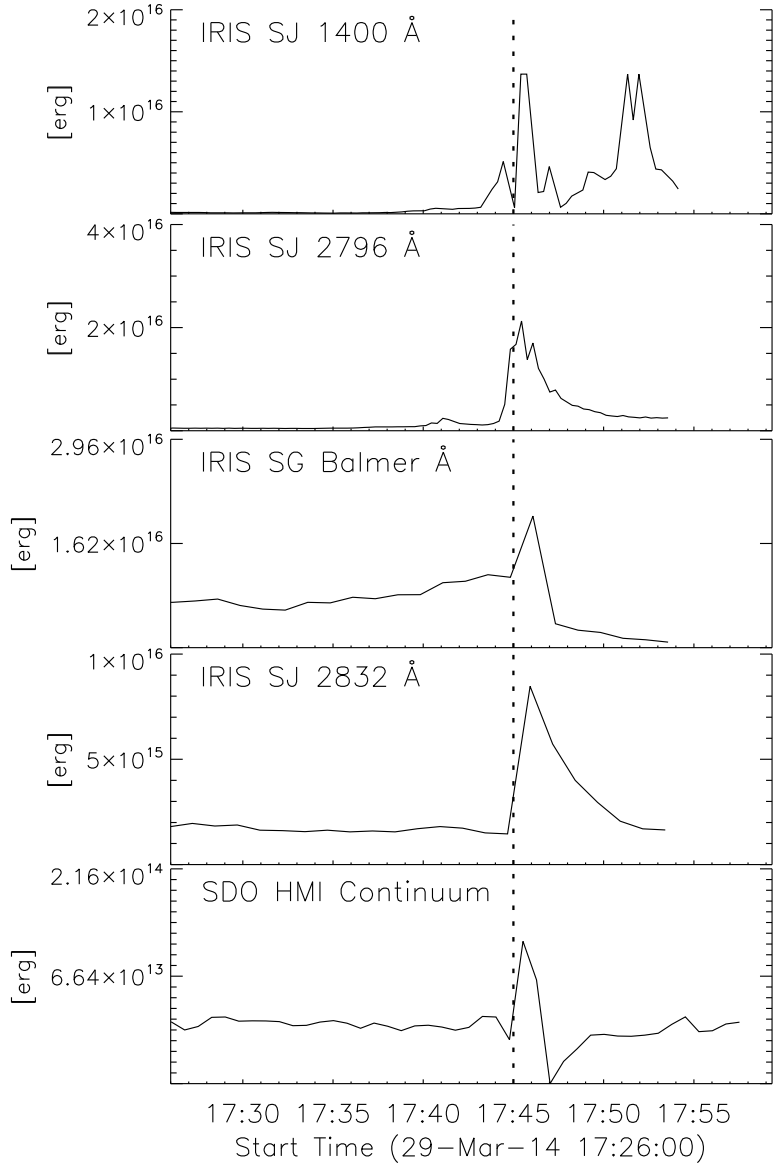

Figure 18: Shows calculated energy (erg) values over time (UT) for the heliocentric coordinates (arcsec) contained in the plot title. Each plot represents an independant data set, in order from top to bottom the sets are; IRIS SJ 1400 Å (Si IV); IRIS SJ 2796 Å (Mg II); IRIS SG 2825.7 to 2825.8 Å (Balmer Continuum);IRIS SJ 2832 Å (Mg II wing); SDO HMI continuum (HMI).

Energy Over Time, Ribbon Location: x = 519, y = 261

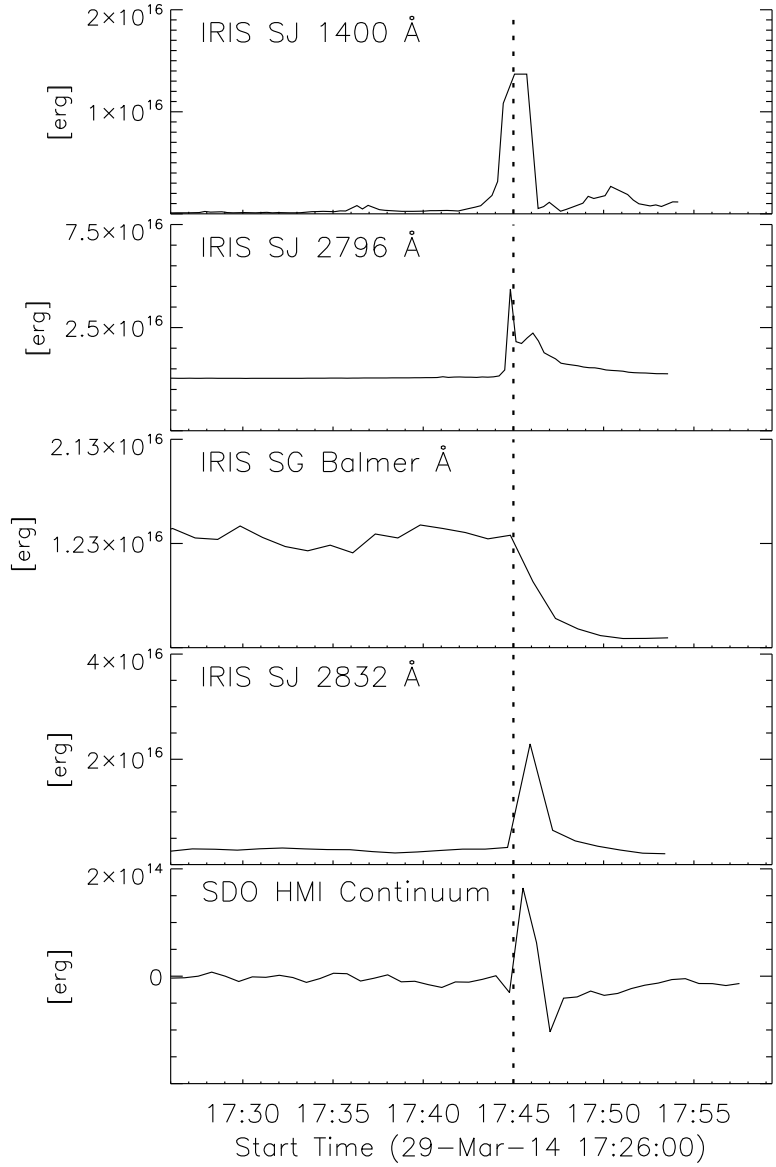

Figure 19: Shows calculated energy (erg) values over time (UT) for the heliocentric coordinates (arcsec) contained in the plot title. Each plot represents an independant data set, in order from top to bottom the sets are; IRIS SJ 1400 Å (Si IV); IRIS SJ 2796 Å (Mg II); IRIS SG 2825.7 to 2825.8 Å (Balmer Continuum);IRIS SJ 2832 Å (Mg II wing); SDO HMI continuum (HMI).

Energy Over Time, Ribbon Location: x = 520, y = 262

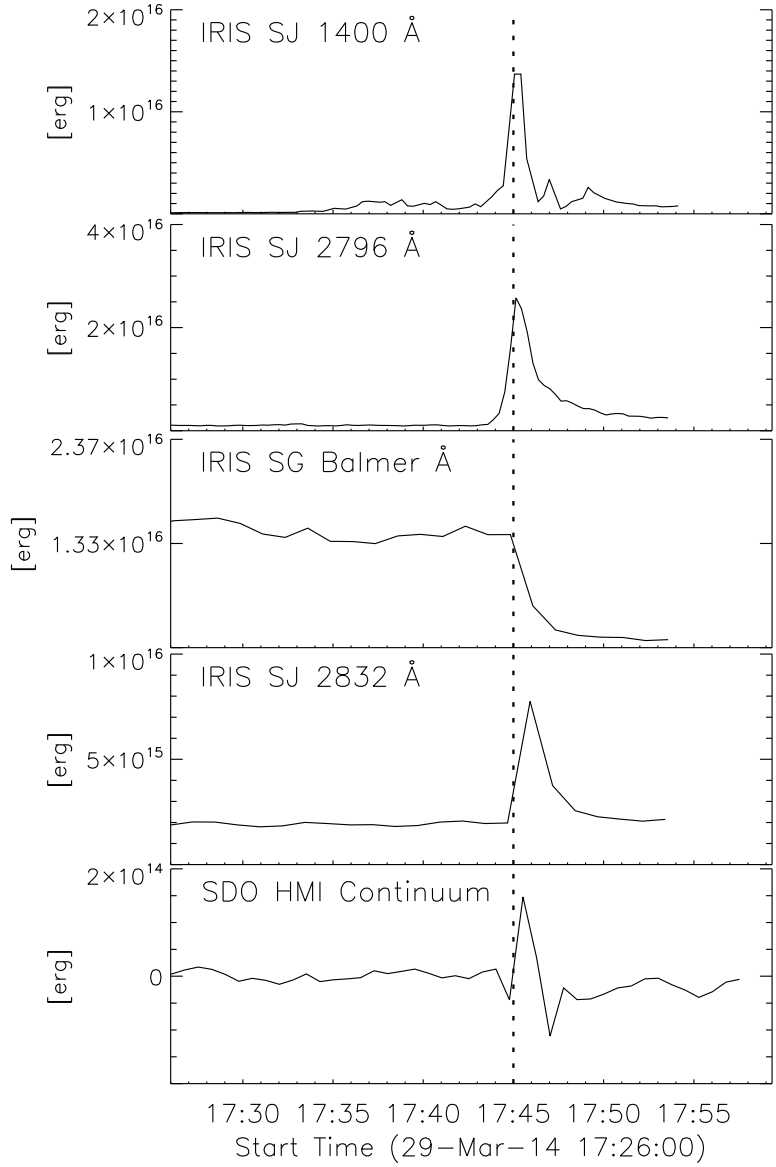

Figure 20: Shows calculated energy (erg) values over time (UT) for the heliocentric coordinates (arcsec) contained in the plot title. Each plot represents an independant data set, in order from top to bottom the sets are; IRIS SJ 1400 Å (Si IV); IRIS SJ 2796 Å (Mg II); IRIS SG 2825.7 to 2825.8 Å (Balmer Continuum);IRIS SJ 2832 Å (Mg II wing); SDO HMI continuum (HMI).

Energy Over Time, Ribbon Location: x = 521, y = 262

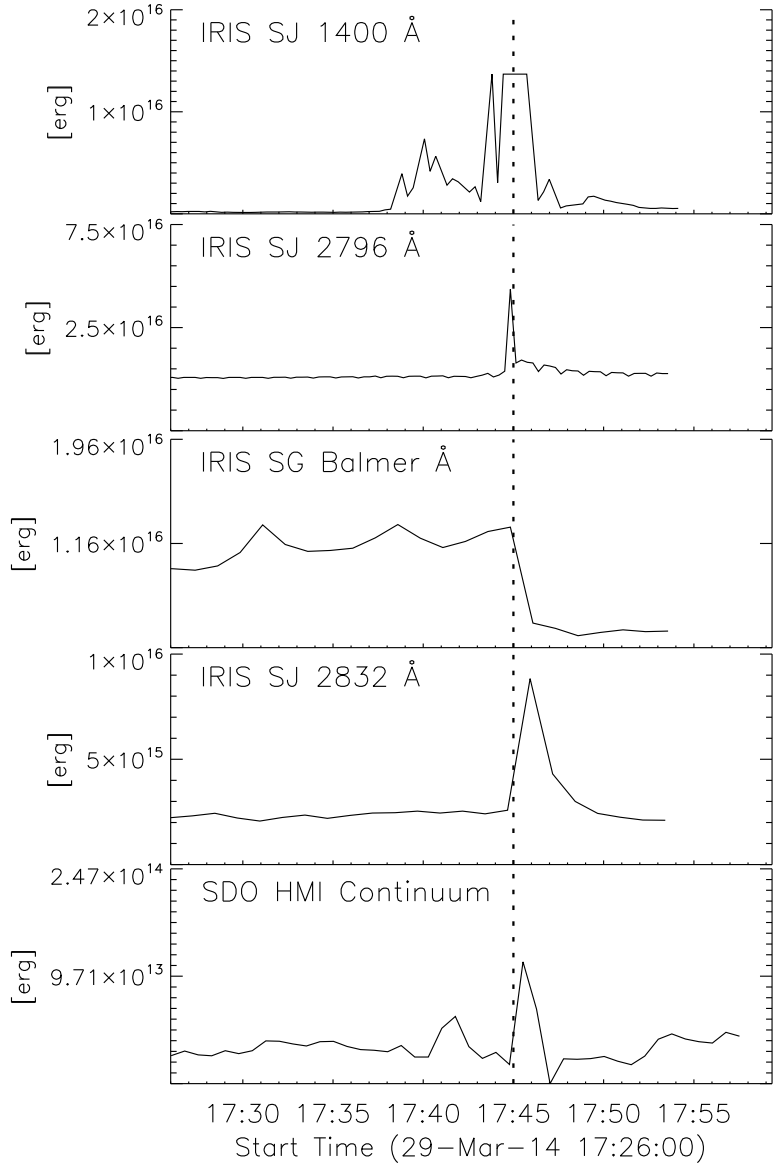

Figure 21: Shows calculated energy (erg) values over time (UT) for the heliocentric coordinates (arcsec) contained in the plot title. Each plot represents an independant data set, in order from top to bottom the sets are; IRIS SJ 1400 Å (Si IV); IRIS SJ 2796 Å (Mg II); IRIS SG 2825.7 to 2825.8 Å (Balmer Continuum);IRIS SJ 2832 Å (Mg II wing); SDO HMI continuum (HMI).

Energy Over Time, Ribbon Location: x = 500, y = 262

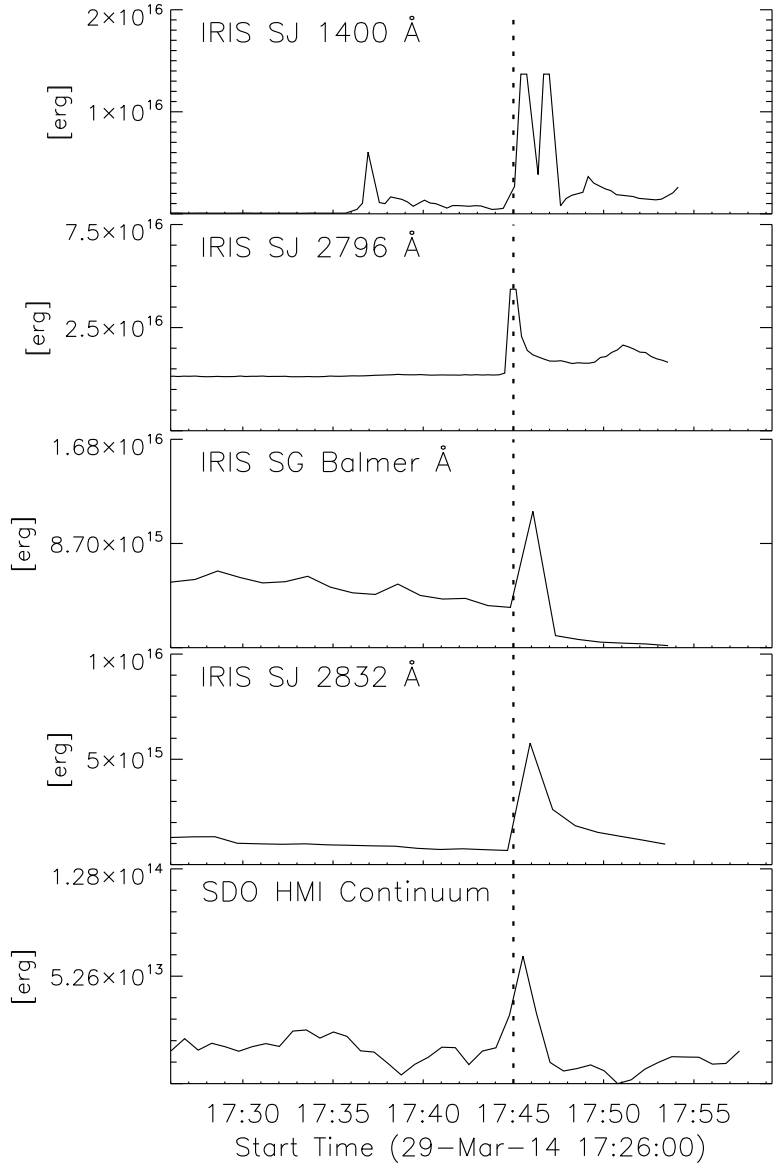

Figure 22: Shows calculated energy (erg) values over time (UT) for the heliocentric coordinates (arcsec) contained in the plot title. Each plot represents an independant data set, in order from top to bottom the sets are; IRIS SJ 1400 Å (Si IV); IRIS SJ 2796 Å (Mg II); IRIS SG 2825.7 to 2825.8 Å (Balmer Continuum);IRIS SJ 2832 Å (Mg II wing); SDO HMI continuum (HMI).

Energy Over Time, Ribbon Location: x = 503, y = 265

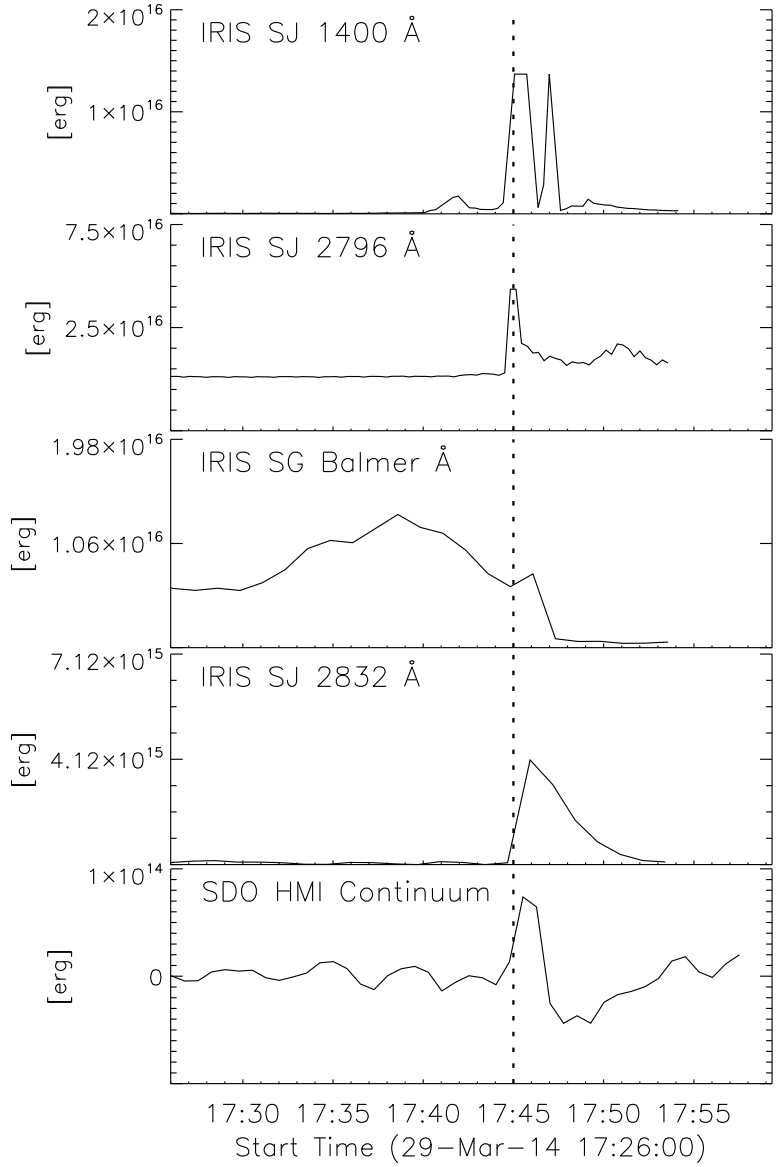

Figure 23: Shows calculated energy (erg) values over time (UT) for the heliocentric coordinates (arcsec) contained in the plot title. Each plot represents an independant data set, in order from top to bottom the sets are; IRIS SJ 1400 Å (Si IV); IRIS SJ 2796 Å (Mg II); IRIS SG 2825.7 to 2825.8 Å (Balmer Continuum);IRIS SJ 2832 Å (Mg II wing); SDO HMI continuum (HMI).

Energy Over Time, Ribbon Location: x = 506, y = 268

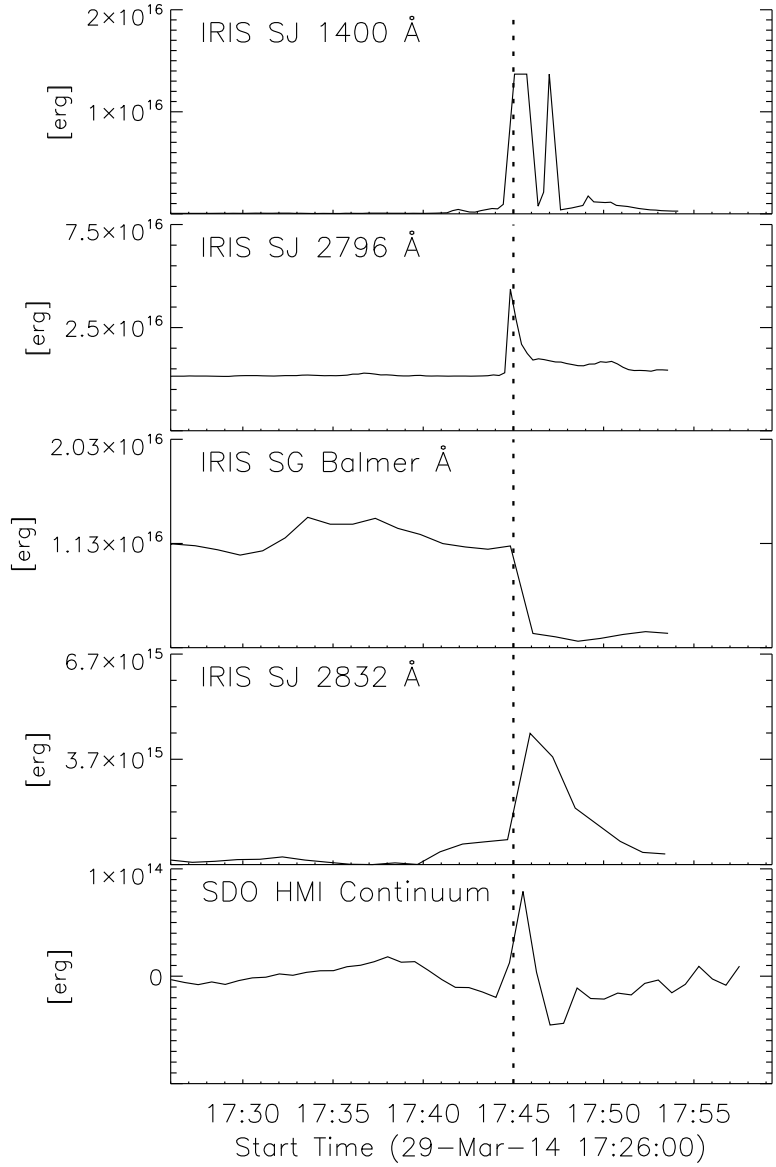

Figure 24: Shows calculated energy (erg) values over time (UT) for the heliocentric coordinates (arcsec) contained in the plot title. Each plot represents an independant data set, in order from top to bottom the sets are; IRIS SJ 1400 Å (Si IV); IRIS SJ 2796 Å (Mg II); IRIS SG 2825.7 to 2825.8 Å (Balmer Continuum);IRIS SJ 2832 Å (Mg II wing); SDO HMI continuum (HMI).

Energy Over Time, Ribbon Location: x = 509, y = 268

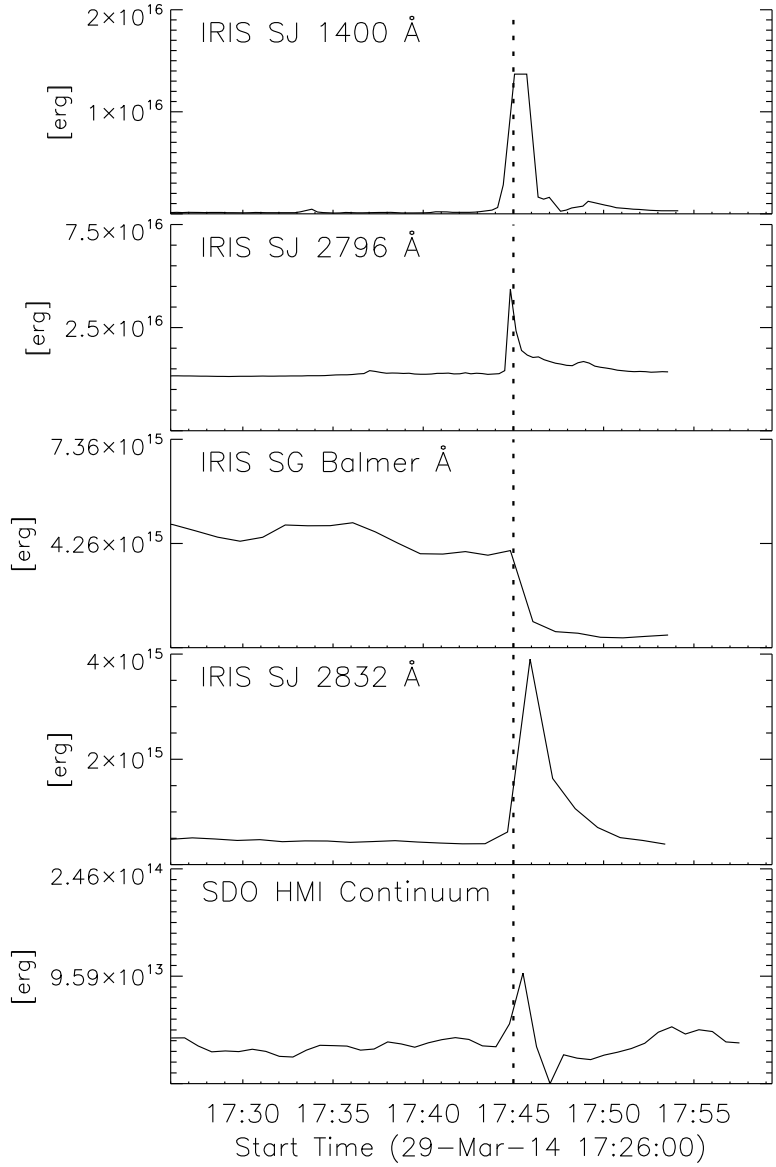

Figure 25: Shows calculated energy (erg) values over time (UT) for the heliocentric coordinates (arcsec) contained in the plot title. Each plot represents an independant data set, in order from top to bottom the sets are; IRIS SJ 1400 Å (Si IV); IRIS SJ 2796 Å (Mg II); IRIS SG 2825.7 to 2825.8 Å (Balmer Continuum);IRIS SJ 2832 Å (Mg II wing); SDO HMI continuum (HMI).

Energy Over Time, Ribbon Location: x = 514, y = 270

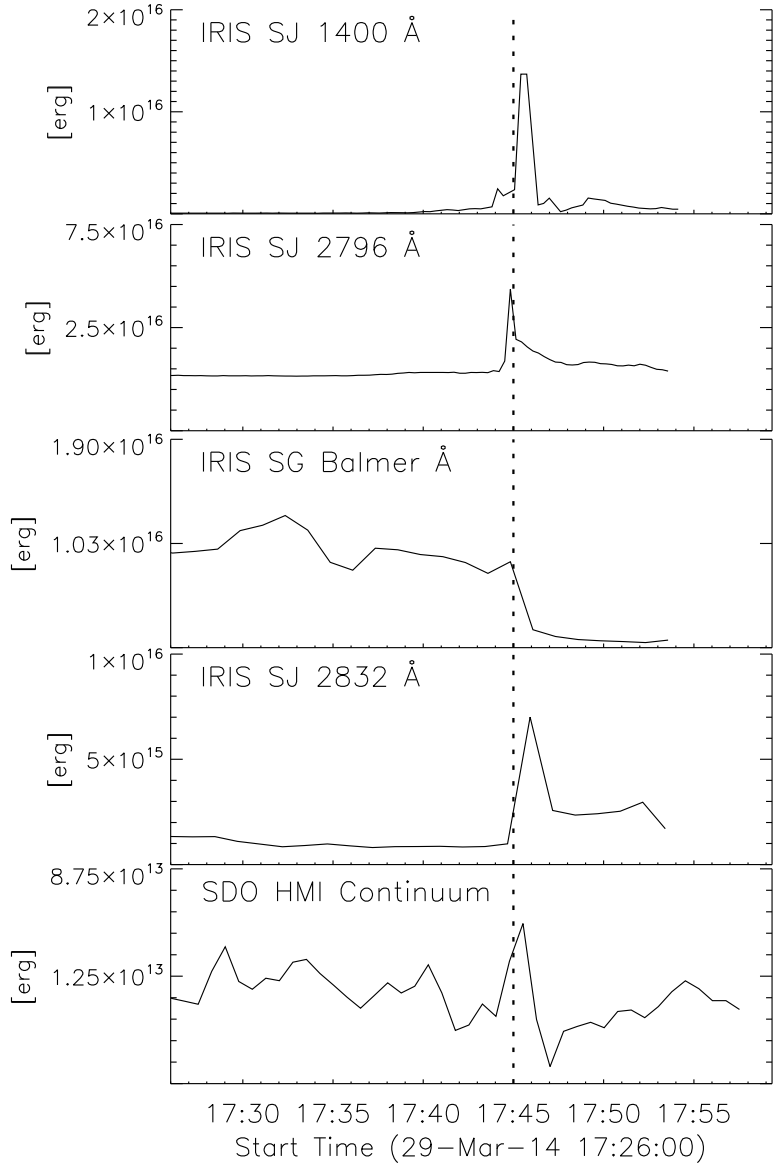

Figure 26: Shows calculated energy (erg) values over time (UT) for the heliocentric coordinates (arcsec) contained in the plot title. Each plot represents an independant data set, in order from top to bottom the sets are; IRIS SJ 1400 Å (Si IV); IRIS SJ 2796 Å (Mg II); IRIS SG 2825.7 to 2825.8 Å (Balmer Continuum);IRIS SJ 2832 Å (Mg II wing); SDO HMI continuum (HMI).

Energy Over Time, Ribbon Location: x = 518, y = 259

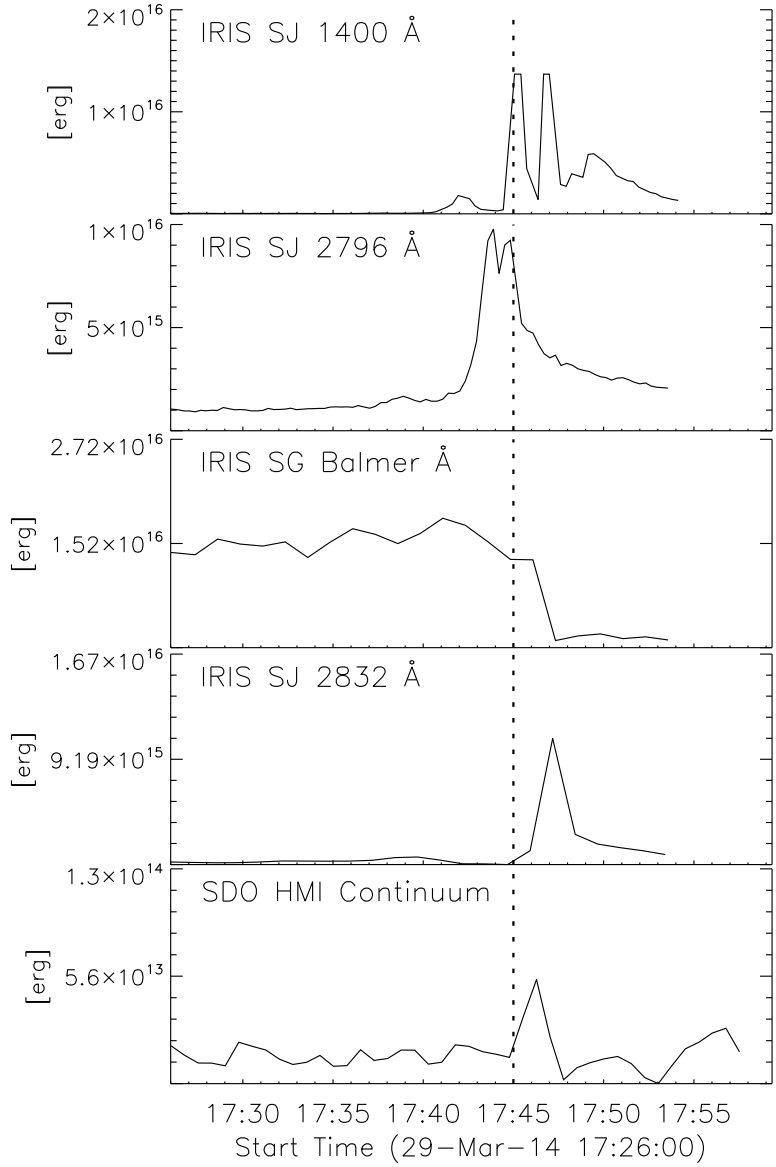

Figure 27: Shows calculated energy (erg) values over time (UT) for the heliocentric coordinates (arcsec) contained in the plot title. Each plot represents an independant data set, in order from top to bottom the sets are; IRIS SJ 1400 Å (Si IV); IRIS SJ 2796 Å (Mg II); IRIS SG 2825.7 to 2825.8 Å (Balmer Continuum);IRIS SJ 2832 Å (Mg II wing); SDO HMI continuum (HMI).

Energy Over Time, Ribbon Location: x = 519, y = 259

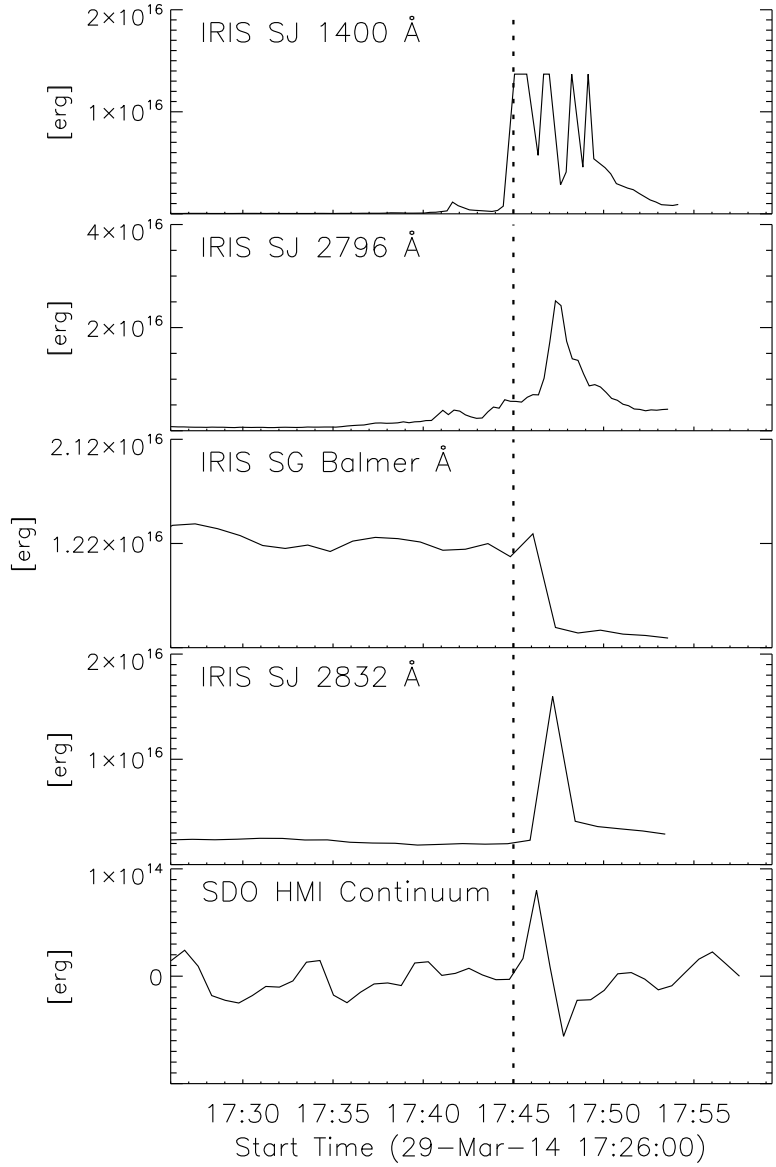

Figure 28: Shows calculated energy (erg) values over time (UT) for the heliocentric coordinates (arcsec) contained in the plot title. Each plot represents an independant data set, in order from top to bottom the sets are; IRIS SJ 1400 Å (Si IV); IRIS SJ 2796 Å (Mg II); IRIS SG 2825.7 to 2825.8 Å (Balmer Continuum);IRIS SJ 2832 Å (Mg II wing); SDO HMI continuum (HMI).

Energy Over Time, Ribbon Location: x = 520, y = 259

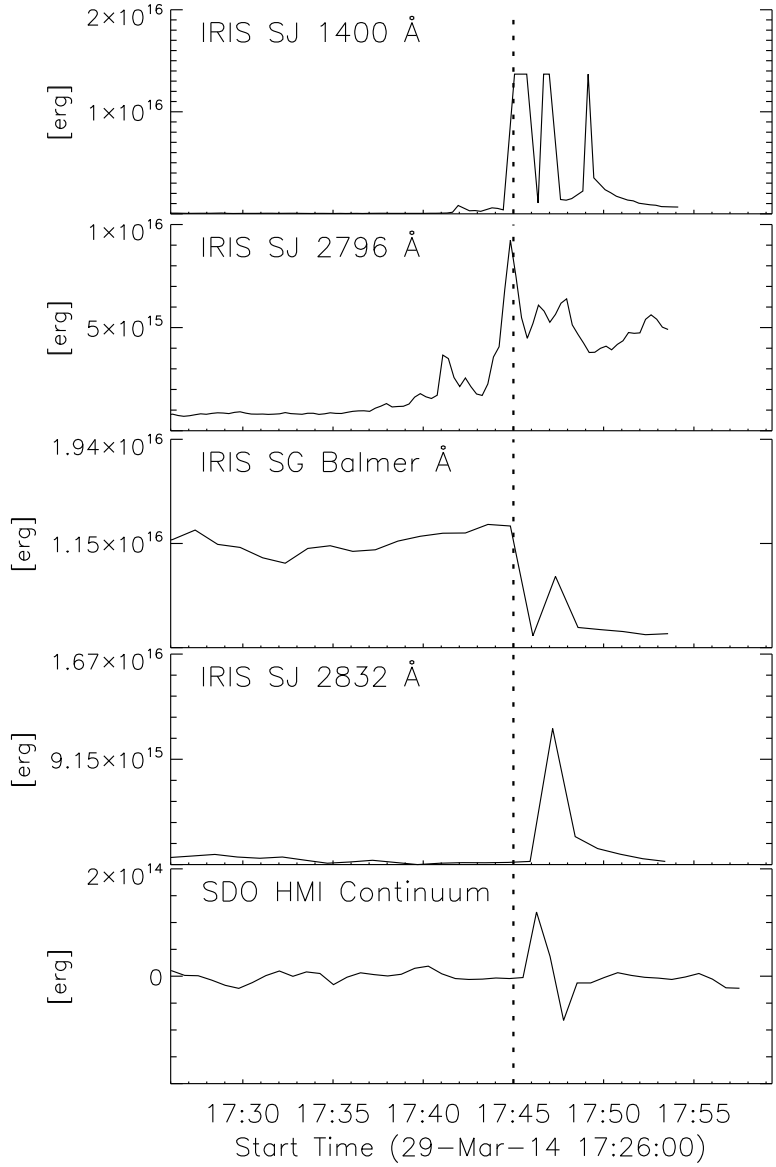

Figure 29: Shows calculated energy (erg) values over time (UT) for the heliocentric coordinates (arcsec) contained in the plot title. Each plot represents an independant data set, in order from top to bottom the sets are; IRIS SJ 1400 Å (Si IV); IRIS SJ 2796 Å (Mg II); IRIS SG 2825.7 to 2825.8 Å (Balmer Continuum);IRIS SJ 2832 Å (Mg II wing); SDO HMI continuum (HMI).

Energy Over Time, Ribbon Location: x = 521, y = 259

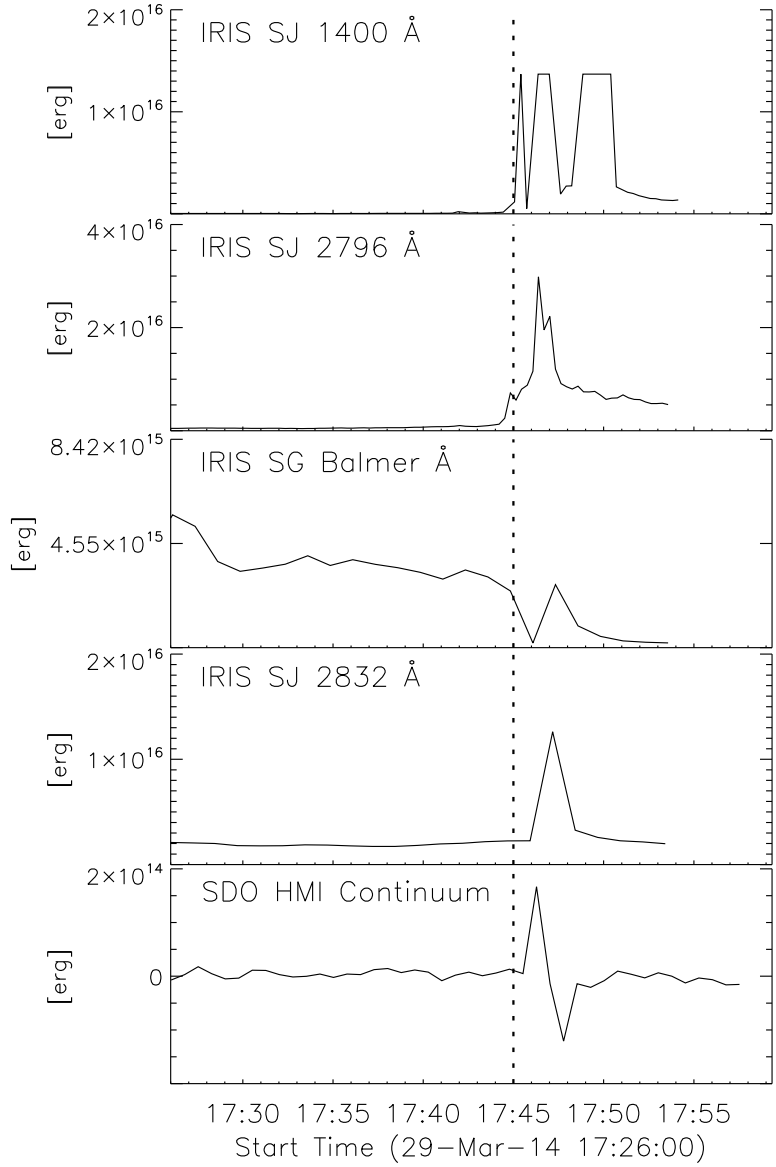

Figure 30: Shows calculated energy (erg) values over time (UT) for the heliocentric coordinates (arcsec) contained in the plot title. Each plot represents an independant data set, in order from top to bottom the sets are; IRIS SJ 1400 Å (Si IV); IRIS SJ 2796 Å (Mg II); IRIS SG 2825.7 to 2825.8 Å (Balmer Continuum);IRIS SJ 2832 Å (Mg II wing); SDO HMI continuum (HMI).

Energy Over Time, Ribbon Location: x = 524, y = 259

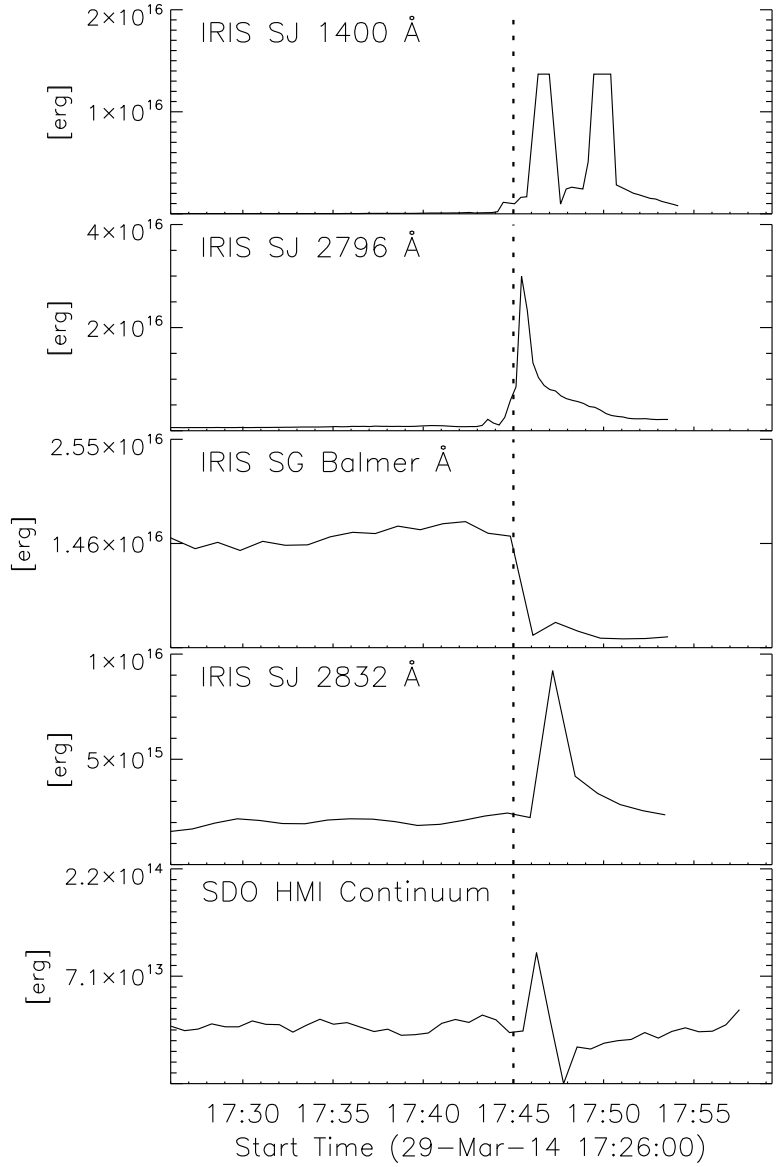

Figure 31: Shows calculated energy (erg) values over time (UT) for the heliocentric coordinates (arcsec) contained in the plot title. Each plot represents an independant data set, in order from top to bottom the sets are; IRIS SJ 1400 Å (Si IV); IRIS SJ 2796 Å (Mg II); IRIS SG 2825.7 to 2825.8 Å (Balmer Continuum);IRIS SJ 2832 Å (Mg II wing); SDO HMI continuum (HMI).

Energy Over Time, Ribbon Location: x = 444, y = 264

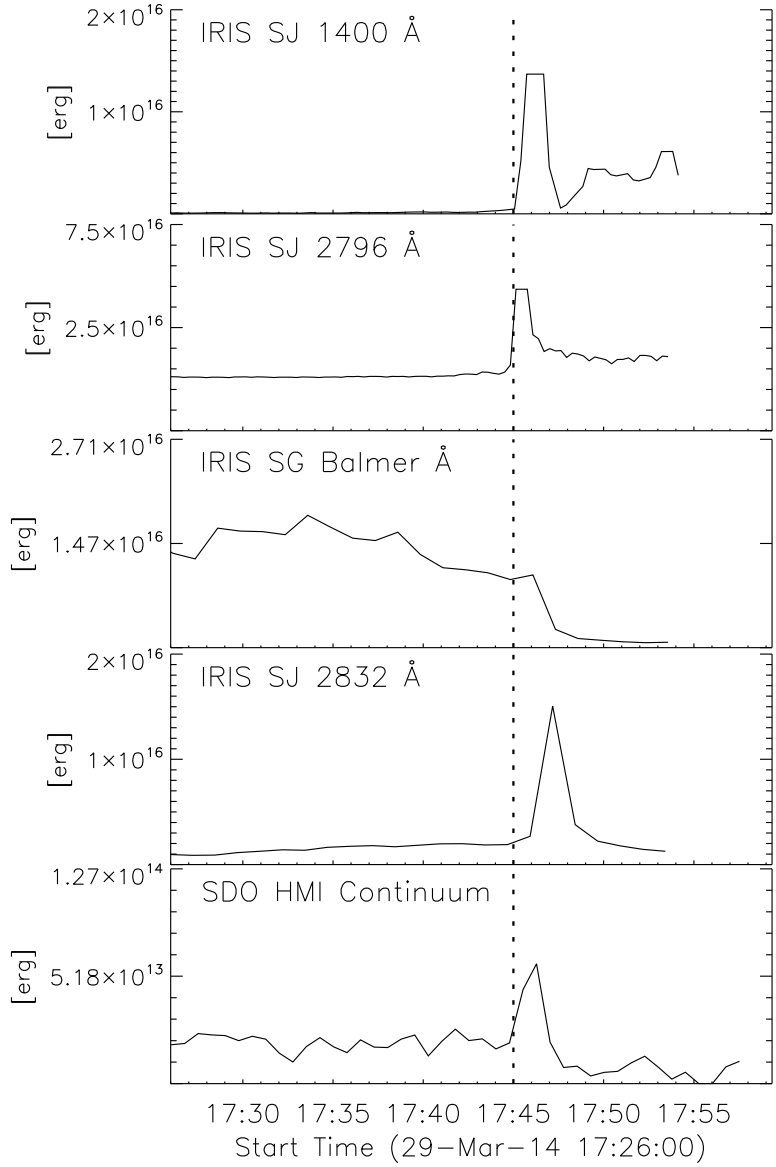

Figure 32: Shows calculated energy (erg) values over time (UT) for the heliocentric coordinates (arcsec) contained in the plot title. Each plot represents an independant data set, in order from top to bottom the sets are; IRIS SJ 1400 Å (Si IV); IRIS SJ 2796 Å (Mg II); IRIS SG 2825.7 to 2825.8 Å (Balmer Continuum);IRIS SJ 2832 Å (Mg II wing); SDO HMI continuum (HMI).

Energy Over Time, Ribbon Location: x = 502, y = 263

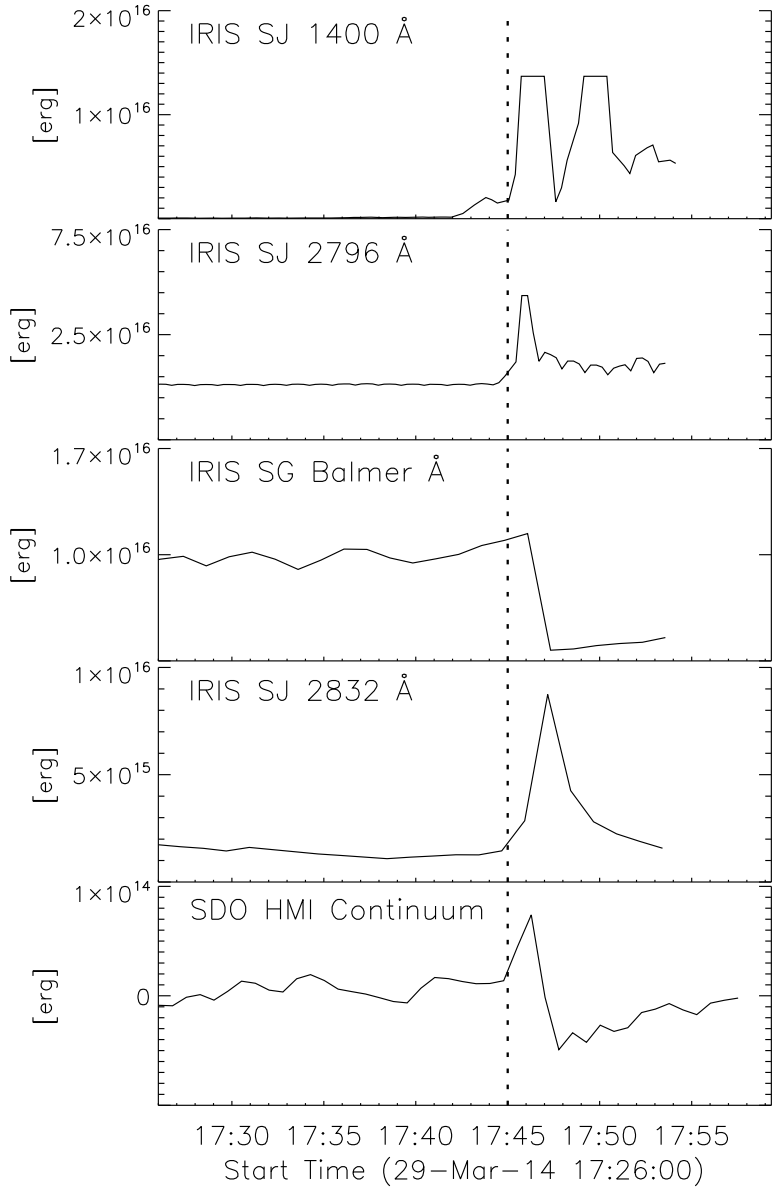

Figure 33: Shows calculated energy (erg) values over time (UT) for the heliocentric coordinates (arcsec) contained in the plot title. Each plot represents an independant data set, in order from top to bottom the sets are; IRIS SJ 1400 Å (Si IV); IRIS SJ 2796 Å (Mg II); IRIS SG 2825.7 to 2825.8 Å (Balmer Continuum);IRIS SJ 2832 Å (Mg II wing); SDO HMI continuum (HMI).

Energy Over Time, Ribbon Location: x = 504, y = 267

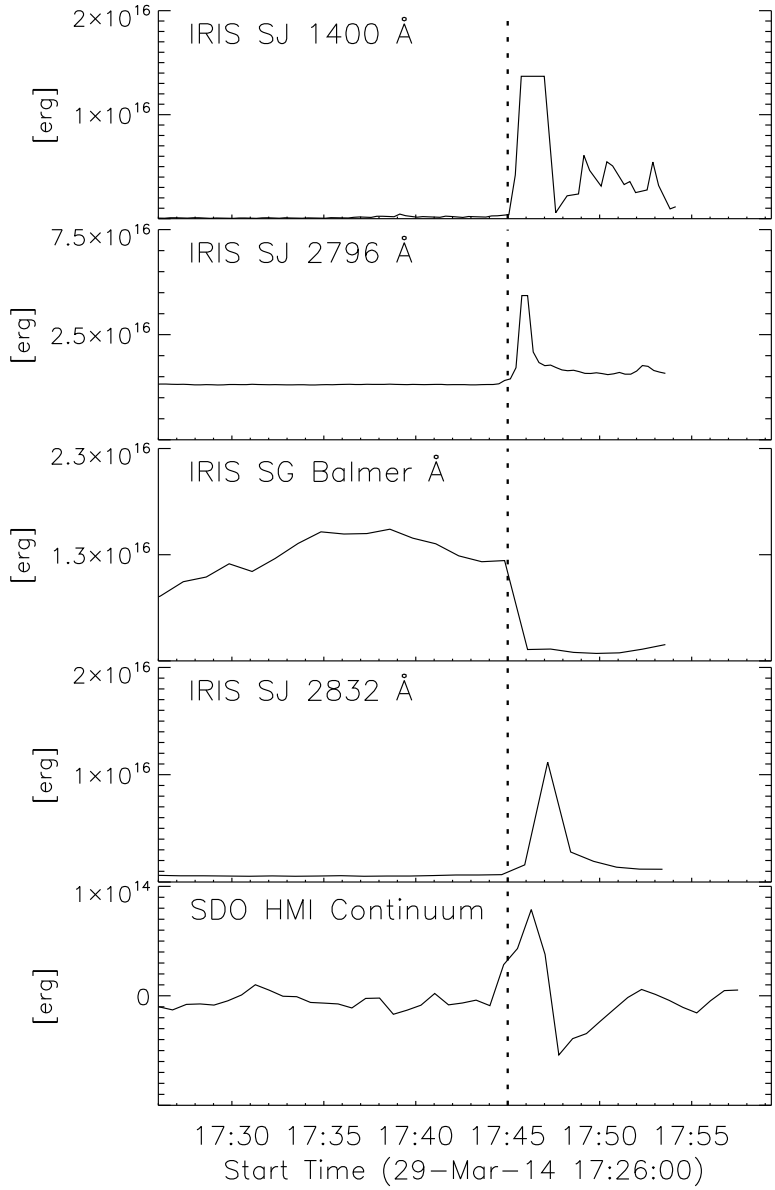

Figure 34: Shows calculated energy (erg) values over time (UT) for the heliocentric coordinates (arcsec) contained in the plot title. Each plot represents an independant data set, in order from top to bottom the sets are; IRIS SJ 1400 Å (Si IV); IRIS SJ 2796 Å (Mg II); IRIS SG 2825.7 to 2825.8 Å (Balmer Continuum);IRIS SJ 2832 Å (Mg II wing); SDO HMI continuum (HMI).

Energy Over Time, Ribbon Location: x = 508, y = 269

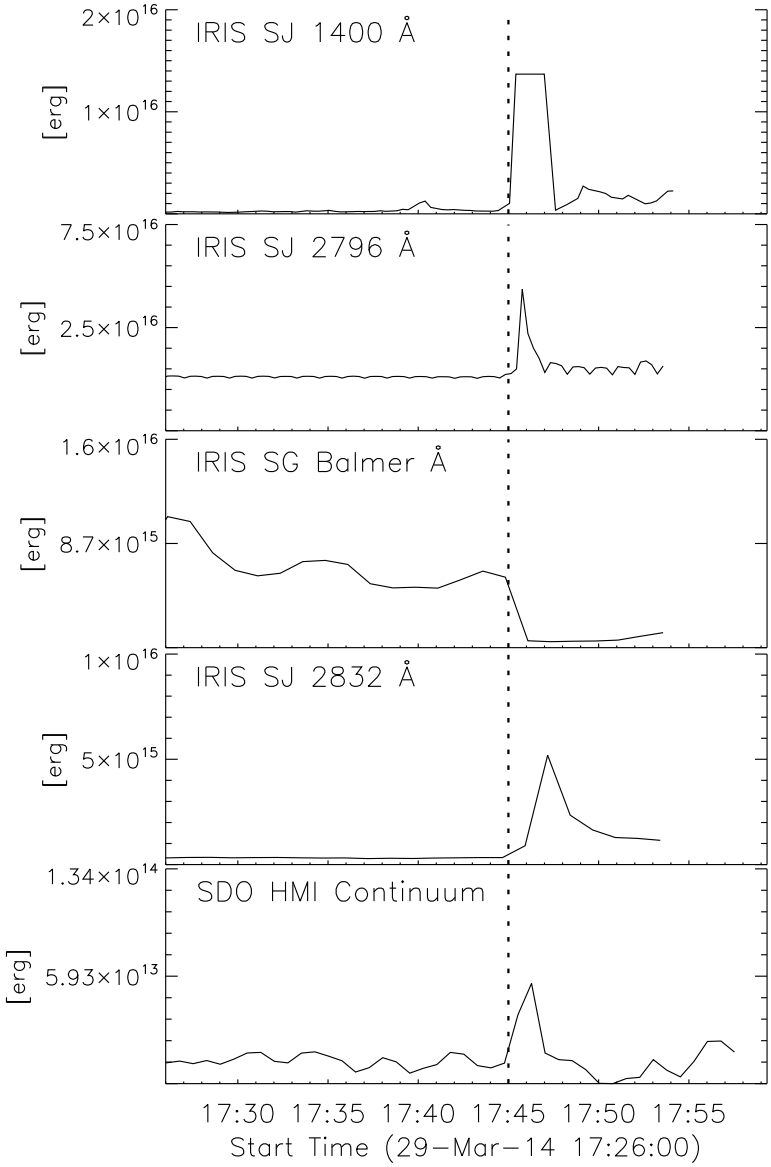

Figure 35: Shows calculated energy (erg) values over time (UT) for the heliocentric coordinates (arcsec) contained in the plot title. Each plot represents an independant data set, in order from top to bottom the sets are; IRIS SJ 1400 Å (Si IV); IRIS SJ 2796 Å (Mg II); IRIS SG 2825.7 to 2825.8 Å (Balmer Continuum);IRIS SJ 2832 Å (Mg II wing); SDO HMI continuum (HMI).

Energy Over Time, Ribbon Location: x = 511, y = 272

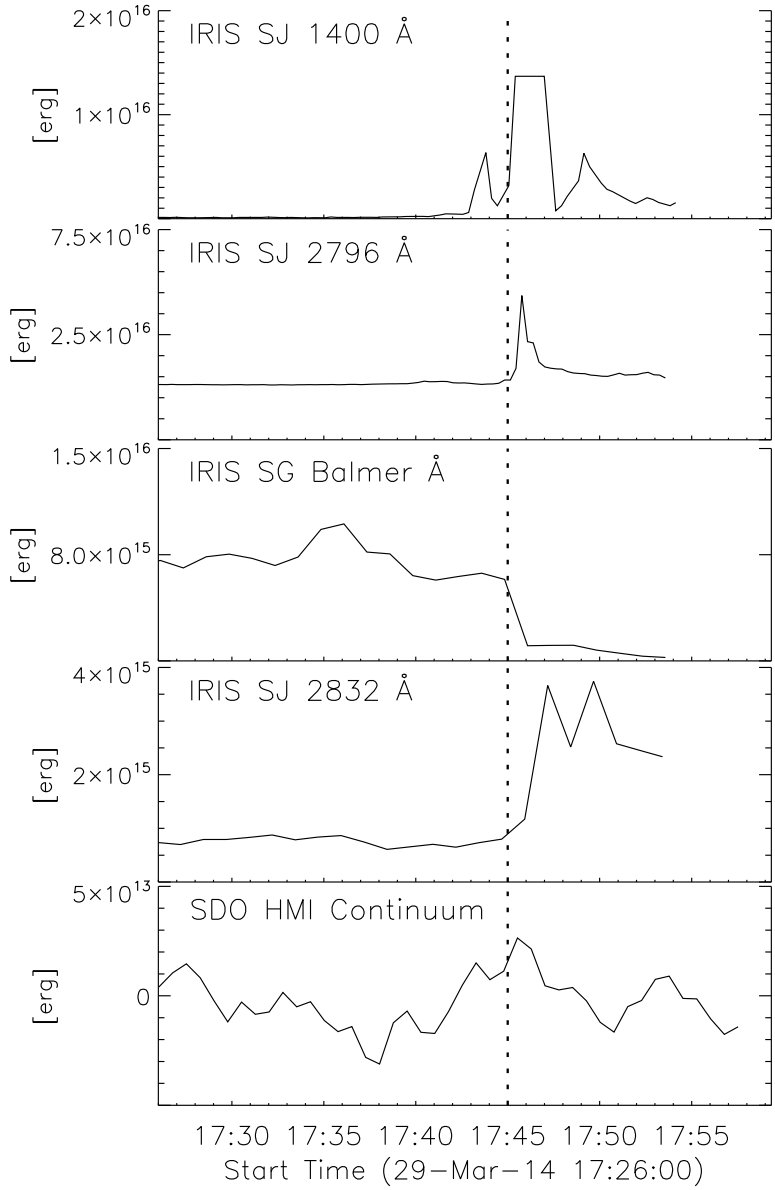

Figure 36: Shows calculated energy (erg) values over time (UT) for the heliocentric coordinates (arcsec) contained in the plot title. Each plot represents an independant data set, in order from top to bottom the sets are; IRIS SJ 1400 Å (Si IV); IRIS SJ 2796 Å (Mg II); IRIS SG 2825.7 to 2825.8 Å (Balmer Continuum);IRIS SJ 2832 Å (Mg II wing); SDO HMI continuum (HMI).

Time UT	Sunquake Coords x",y"	E_{SiIV}	E_{MgII}	E_{Balm}	E_{MgIIw}	E_{HMI}	E_{area}
17:45	518.5, 264.0	9.63E+14	4.36E+16	2.68E+16	8.21E+15	3.29E+13	2.54E+17
17:46	518.5, 264.0	2.52E+15	1.58E+16	5.00E+15	5.31E+15	3.18E+13	2.51E+17

Table 4: Pixel coordinates in arcsecs and Energies in ergs at 17:45 and 17:46 for the sunquake pixel and area. *coordinates are the central pixel of a 13 pixel sunquake area

Time	Si Coords (x,y)	E_{SiIV}	Mg Coords(x,y)	E_{MgII}	Balm Coords(x,y)	E_{Balm}	Mgw Coords (x,y)	E_{MgIIw}	HMI Coords (x,y)	E_{HMI}
17:45	517.54, 261.58	1.78E+15	496.03, 263.76	2.34E+16	517.80, 260.50	1.26E+16	517.14, 261.79	9.32E+15	517.80, 260.50	5.83E+13
17:45	517.54, 264.13	5.93E+14	502.50, 264.93	1.58E+16	518.80, 261.00	1.97E+16	518.68, 262.86	8.47E+15	518.80, 261.00	1.15E+14
17:45	518.02, 266.35	1.37E+16	504.66, 268.10	4.36E+16	519.70, 261.70	8.93E+15	519.61, 263.79	2.29E+16	519.70, 261.70	1.64E+14
17:45	519.29, 267.78	1.37E+16	509.13, 269.64	1.58E+16	520.60, 262.30	7.01E+15	521.15, 264.87	7.76E+15	520.60, 262.30	1.48E+14
17:45	522.31, 267.14	1.37E+16	514.09, 271.49	4.36E+16	521.70, 262.60	5.51E+15	523.46, 265.18	8.83E+15	521.70, 262.60	1.17E+14
17:45	496.03, 264.56	2.69E+15	517.48, 262.95	4.36E+16	500.70, 262.70	1.12E+16	496.03, 264.56	5.77E+15	500.70, 262.70	6.66E+13
17:45	502.20, 265.18	1.37E+16	518.60, 264.07	4.36E+16	503.80, 265.00	7.97E+15	502.20, 265.18	4.10E+15	503.80, 265.00	7.39E+13
17:45	504.66, 268.10	1.37E+16	519.44, 265.75	4.36E+16	506.90, 268.10	3.48E+15	504.66, 268.10	4.43E+15	506.90, 268.10	7.90E+13
17:45	509.13, 269.64	1.37E+16	520.55, 266.86	4.36E+16	509.28, 268.79	1.94E+15	509.13, 269.64	3.90E+15	509.28, 268.79	1.00E+14
17:45	513.29, 271.65	2.37E+15	524.47, 265.47	4.36E+16	514.40, 270.10	3.17E+15	513.29, 271.65	7.01E+15	514.40, 270.10	4.93E+13
17:46	499.88, 264.87	1.39E+15	486.52, 264.28	4.85E+15	518.60, 259.10	4.08E+15	517.91, 260.40	1.07E+16	518.60, 259.10	5.33E+13
17:46	502.35, 266.56	5.73E+15	497.24, 265.62	6.50E+15	519.60, 259.30	5.03E+15	519.76, 259.94	1.60E+16	519.60, 259.30	7.99E+13
17:46	503.89, 268.57	1.06E+15	500.22, 267.63	4.48E+15	520.60, 259.50	9.00E+15	521.77, 259.47	1.14E+16	520.60, 259.50	1.20E+14
17:46	506.97, 270.72	1.37E+16	505.29, 269.47	8.83E+15	521.60, 259.90	3.02E+15	523.77, 258.86	1.26E+16	521.60, 259.90	1.67E+14
17:46	511.29, 272.11	1.37E+16	512.73, 271.15	2.33E+16	524.10, 259.70	6.31E+15	524.69, 260.24	9.22E+15	524.10, 259.70	1.04E+14
17:46	515.18, 261.86	1.37E+16	517.98, 261.31	4.36E+16	499.10, 264.70	4.50E+15	499.88, 264.87	1.51E+16	499.10, 264.70	6.05E+13
17:46	517.70, 261.58	1.37E+16	519.09, 261.31	4.36E+16	502.10, 263.80	3.60E+15	502.35, 266.56	8.74E+15	502.10, 263.80	7.39E+13
17:46	520.21, 262.41	1.37E+16	521.33, 261.31	4.36E+16	504.60, 267.00	3.95E+15	503.89, 268.57	1.12E+16	504.60, 267.00	7.88E+13
17:46	523.28, 262.97	1.37E+16	522.73, 261.31	4.36E+16	508.40, 269.80	2.03E+15	506.97, 270.72	5.20E+15	508.40, 269.80	5.43E+13
17:46	525.52, 263.81	1.37E+16	524.68, 262.99	4.36E+16	511.00, 272.00	1.95E+15	511.29, 272.11	3.66E+15	511.00, 272.00	2.14E+13

Table 5: Coordinates and Energies at 17:45 and 17:46 for ribbon sample locations.

References

M. J. Aschwanden, A. O. Benz, B. R. Dennis, and R. A. Schwartz. Solar Electron Beams Detected in Hard X-Rays and Radio Waves. ApJ, 455:347, December 1995. doi: 10.1086/176582.

P. Boerner, C. Edwards, J. Lemen, A. Rausch, C. Schrijver, R. Shine, L. Shing, R. Stern, T. Tarbell, A. Title, C. J. Wolfson, R. Soufli, E. Spiller, E. Gullikson, D. McKenzie, D. Windt, L. Golub, W. Podgorski, P. Testa, and M. Weber. Initial Calibration of the Atmospheric Imaging Assembly (AIA) on the Solar Dynamics Observatory (SDO). Sol. Phys., 275:41–66, January 2012. doi: 10.1007/s11207-011-9804-8.

D. C. Braun, C. Lindsey, Y. Fan, and S. M. Jefferies. Local acoustic diagnostics of the solar interior. ApJ, 392: 739–745, June 1992. doi: 10.1086/171477.

J. C. Brown. The Deduction of Energy Spectra of Non-Thermal Electrons in Flares from the Observed Dynamic Spectra of Hard X-Ray Bursts. Sol. Phys., 18:489–502, July 1971. doi: 10.1007/BF00149070.

H. Carmichael. A Process for Flares. *NASA Special Publication*, 50:451, 1964.

S. Couvidat, J. Schou, R. A. Shine, R. I. Bush, J. W. Miles, P. H. Scherrer, and R. L. Rairden. Wavelength Dependence of the Helioseismic and Magnetic Imager (HMI) Instrument onboard the Solar Dynamics Observatory (SDO). Sol. Phys., 275:285–325, January 2012. doi: 10.1007/s11207-011-9723-8.

B. De Pontieu, A. M. Title, J. R. Lemen, G. D. Kushner, D. J. Akin, B. Allard, T. Berger, P. Boerner, M. Cheung, C. Chou, J. F. Drake, D. W. Duncan, S. Freeland, G. F. Heyman, C. Hoffman, N. E. Hurlburt, R. W. Lindgren, D. Mathur, R. Rehse, D. Sabolish, R. Seguin, C. J. Schrijver, T. D. Tarbell, J.-P. Wülser, C. J. Wolfson, C. Yanari, J. Mudge, N. Nguyen-Phuc, R. Timmons, R. van Bezooijen, I. Weingrod, R. Brookner, G. Butcher, B. Dougherty, J. Eder, V. Knagenhjelm, S. Larsen, D. Mansir, L. Phan, P. Boyle, P. N. Cheimets, E. E. DeLuca, L. Golub, R. Gates, E. Hertz, S. McKillop, S. Park, T. Perry, W. A. Podgorski, K. Reeves, S. Saar, P. Testa, H. Tian, M. Weber, C. Dunn, S. Eccles, S. A. Jaeggli, C. C. Kankelborg, K. Mashburn, N. Pust, L. Springer, R. Carvalho, L. Kleint, J. Marmie, E. Mazmanian, T. M. D. Pereira, S. Sawyer, J. Strong, S. P. Worden, M. Carlsson, V. H. Hansteen, J. Leenaarts, M. Wiesmann, J. Aloise, K.-C. Chu, R. I. Bush, P. H. Scherrer, P. Brekke, J. Martinez-Sykora, B. W. Lites, S. W. McIntosh, H. Uitenbroek, T. J. Okamoto, M. A. Gummin, G. Auker, P. Jerram, P. Pool, and N. Waltham. The Interface Region Imaging Spectrograph (IRIS). Sol. Phys., 289:2733–2779, July 2014. doi: 10.1007/s11207-014-0485-y.

M. D. Ding. The Origin of Solar White-Light Flares. In P. Heinzel, I. Dorotovič, and R. J. Rutten, editors, *The Physics of Chromospheric Plasmas*, volume 368 of *Astronomical Society of the Pacific Conference Series*, page 417, May 2007.

A.-C. Donea and C. Lindsey. Seismic Emission from the Solar Flares of 2003 October 28 and 29. ApJ, 630: 1168–1183, September 2005. doi: 10.1086/432155.

A.-C. Donea, D. C. Braun, and C. Lindsey. Seismic Images of a Solar Flare. ApJ, 513:L143–L146, March 1999. doi: 10.1086/311915.

T. L. Duvall, Jr., S. M. Jefferies, J. W. Harvey, and M. A. Pomerantz. Time-distance helioseismology. Nature, 362:430–432, April 1993. doi: 10.1038/362430a0.

B. N. Dwivedi and F. b. E. N. Parker. *Dynamic Sun*. Cambridge University Press, Cambridge, UK, May 2003.

L. Fletcher. Ultra-violet footpoints as tracers of coronal magnetic connectivity and restructuring during a solar flare. A&A, 493:241–250, January 2009. doi: 10.1051/0004-6361:20077972.

P. V. Foukal. *Solar Astrophysics, 2nd, Revised Edition*. Wiley-VCH, 2004.

T. Hirayama. Theoretical Model of Flares and Prominences. I: Evaporating Flare Model. Sol. Phys., 34:323–338, February 1974. doi: 10.1007/BF00153671.

H. S. Hudson. Implosions in Coronal Transients. ApJ, 531:L75–L77, March 2000. doi: 10.1086/312516.

H. S. Hudson, G. H. Fisher, and B. T. Welsch. Flare Energy and Magnetic Field Variations. In R. Howe, R. W. Komm, K. S. Balasubramaniam, and G. J. D. Petrie, editors, *Subsurface and Atmospheric Influences on Solar Activity*, volume 383 of *Astronomical Society of the Pacific Conference Series*, page 221, 2008.

P. G. Judge, L. Kleint, A. Donea, A. Sainz Dalda, and L. Fletcher. On the Origin of a Sunquake during the 2014 March 29 X1 Flare. ApJ, 796:85, December 2014. doi: 10.1088/0004-637X/796/2/85.

G. S. Kerr and L. Fletcher. Physical Properties of White-light Sources in the 2011 February 15 Solar Flare. ApJ, 783:98, March 2014. doi: 10.1088/0004-637X/783/2/98.

R. A. Kopp and G. W. Pneuman. Magnetic reconnection in the corona and the loop prominence phenomenon. Sol. Phys., 50:85–98, October 1976. doi: 10.1007/BF00206193.

A. G. Kosovichev. Sunquakes: helioseismic response to solar flares. *ArXiv e-prints*, February 2014.

A. G. Kosovichev and V. V. Zharkova. Seismic Response to Solar Flares: Theoretical Predictions. In *Helioseismology*, volume 376 of *ESA Special Publication*, page 341, 1995.

A. G. Kosovichev and V. V. Zharkova. X-ray flare sparks quake inside Sun. Nature, 393:317–318, May 1998. doi: 10.1038/30629.

A. G. Kosovichev and V. V. Zharkova. Magnetic Energy Release and Transients in the Solar Flare of 2000 July 14. ApJ, 550:L105–L108, March 2001. doi: 10.1086/319484.

C. Lindsey and D. C. Braun. Helioseismic imaging of sunspots at their antipodes. Sol. Phys., 126:101–115, March 1990. doi: 10.1007/BF00158301.

C. Lindsey and D. C. Braun. Helioseismic Holography. ApJ, 485:895–903, August 1997.

M. E. Machado, A. G. Emslie, and E. H. Avrett. Radiative backwarming in white-light flares. Sol. Phys., 124: 303–317, September 1989. doi: 10.1007/BF00156272.

J. C. Martínez-Oliveros and A.-C. Donea. Magnetic field variations and seismicity of solar active regions. MNRAS, 395:L39–L42, May 2009. doi: 10.1111/j.1745-3933.2009.00637.x.

J. C. Martínez-Oliveros, H. Moradi, and A.-C. Donea. Seismic Emissions from a Highly Impulsive M6.7 Solar Flare. Sol. Phys., 251:613–626, September 2008. doi: 10.1007/s11207-008-9122-y.

E. Pedram and S. A. Matthews. A Survey of the Hard X-Ray Characteristics of Seismically Active and Quiet White-Light Flares. Sol. Phys., 277:317–335, April 2012. doi: 10.1007/s11207-011-9922-3.

F. Roddier. Principle of production of an acoustic hologram of the solar surface. *Academie des Sciences Paris Comptes Rendus Serie B Sciences Physiques*, 281:93–95, July 1975.

K. Shibata and T. Magara. Solar Flares: Magnetohydrodynamic Processes. *Living Reviews in Solar Physics*, 8:6, December 2011. doi: 10.12942/lrsp-2011-6.

P. A. Sturrock. Model of the High-Energy Phase of Solar Flares. Nature, 211:695–697, August 1966. doi: 10.1038/211695a0.

C. L. Wolff. Free Oscillations of the Sun and Their Possible Stimulation by Solar Flares. ApJ, 176:833, September 1972. doi: 10.1086/151680.

S. Zharkov, L. M. Green, S. A. Matthews, and V. V. Zharkova. 2011 February 15: Sunquakes Produced by Flux Rope Eruption. ApJ, 741:L35, November 2011. doi: 10.1088/2041-8205/741/2/L35.

S. Zharkov, L. M. Green, S. A. Matthews, and V. V. Zharkova. Properties of the 15 February 2011 Flare Seismic Sources. Sol. Phys., 284:315–327, June 2013. doi: 10.1007/s11207-012-0169-4.

V. V. Zharkova and S. I. Zharkov. On the Origin of Three Seismic Sources in the Proton-rich Flare of 2003 October 28. ApJ, 664:573–585, July 2007. doi: 10.1086/518731.